Phase reconfiguration of multivalent nickel sulfides in hydrogen evolution

Yu Sun
University of Science and Technology Beijing

Jing Wu
University of Science and Technology Beijing

Zheng Zhang
University of Science and Technology Beijing

Qingliang Liao
University of Science and Technology Beijing

Suicai Zhang
University of Science and Technology Beijing

Xin Wang
University of Science and Technology Beijing

Baishan Liu
University of Science and Technology Beijing

Yunqi Zhao
University of Science and Technology Beijing

Yong Xie
University of Science and Technology Beijing

Kaikai Ma
University of Science and Technology Beijing

Zhuo Kang
University of Science and Technology Beijing

Yue Zhang (✉ yuezhang@ustb.edu.cn)
University of Science and Technology Beijing   https://orcid.org/0000-0002-8213-1420

Article

Version of Record: A version of this preprint was published at Energy & Environmental Science on January 1st, 2022. See the published version at https://doi.org/10.1039/D1EE02985A.

Phase reconfiguration of multivalent nickel sulfides in hydrogen evolution

Yu Sun[1,2,3], Jing Wu[1,2,3], Zheng Zhang[1,2,3], Qingliang Liao[1,2], Suicai Zhang[1,2], Xin Wang[1,2], Baishan Liu[1,2], Yunqi Zhao[1,2], Yong Xie[1,2], Kaikai Ma[1,2], Zhuo Kang[*][1,2] and Yue Zhang[*][1,2]

[1]Beijing Advanced Innovation Center for Materials Genome Engineering, Beijing Key Laboratory for Advanced Energy Materials and Technologies, University of Science and Technology Beijing, Beijing 100083, China

[2]State Key Laboratory for Advanced Metals and Materials, School of Materials Science and Engineering, University of Science and Technology Beijing, Beijing 100083, China

[3]These authors contributed equally: Yu Sun, Jing Wu, Zheng Zhang.

*e-mail: zhuokang@ustb.edu.cn; yuezhang@ustb.edu.cn

Abstract：Deciphering the dynamic evolution of catalysts' atomic and electronic structure in operating conditions is pivotal for unraveling the activity origin and improving catalyst design. Earth-abundant transition metal catalysts have shown efficient catalytic efficiency and are attractive due to sustainable and economic considerations. However, the dynamic evolution process during their whole service time remains elusive, which is greatly complicated by the multiple component and valence states as well as the structural complexity of materials. Here in this work, we investigated the atomic-scale evolution of multivalent nickel-based sulfides (from NiS_2 to α-NiS, β-NiS and Ni_3S_4) as model catalysts for hydrogen evolution reaction (HER), via operando Raman and X-ray absorption spectroscopies corroborated by theoretical calculations. Dynamic reconstruction propagating from surface to bulk, mediated by sulphur vacancy, has been demonstrated for these materials, all with the terminated Ni_3S_2 phase on catalyst surface being responsible for subsequent catalysis. Partial Fe substitution prompts such reconfiguration process and hence improves HER performance, which establishes the dynamic working mechanism of widely-adopted doping strategy. We unprecedentedly reveal the dynamic reconstruction with lower valence state tendency of transition metals in the catalytically terminated phase during HER, and the life-time dynamic correlation between structure and activity, providing insights into future catalyst design.

Introduction

Electrocatalytic water splitting to extract oxygen and hydrogen is expected to play an important role to replace fossil fuels in future sustainable energy supply[1-4]. Earth-abundant multivalent transition metal compounds have shown comparable activities to precious metal

based catalysts, and have attracted increasing attention. Recent reports found that they are prone to involve several surface reconstruction process under complex conditions of catalytic reactions, including the crystal plane alternation[5,6], atom segregation[7,8], ligand dissociation[9], coordination tailoring[10,11], and even the phase transition for bulk structure[6,12,13]. However, the multiple component and valence state, as well as the structural complexity of these materials greatly complicate the dynamic reconstruction process, inducing the ambiguity about the decisive role of active state in catalytic process. Thus, it is imperative to investigate the reaction process under catalytically relevant conditions via operando characterization technologies to reveal the corresponding evolution law, and bridge the gap between theoretical design and practical application for catalysts.

Recently, in terms of water oxidation catalysts, the dynamic reconstruction process has been well documented to transform to the catalytically authentic active state of oxyhydroxides, for layered double hydroxide[14-18], spinel[19] and perovskite[20] catalysts. Various engineering strategies have been designed to stimulate such phase transformation process[21,22] and optimize the surface atomic ordering[15] and electronic structure of resulted catalytic active phase[23], together with unveiling feasible catalytic pathways[24], which promote the water oxidation performance. With regard to hydrogen evolution reaction (HER) electrochemical environment, since the preliminarily noted discovery of the reconstructed CoS_2 on amorphous cobalt sulfide catalyst[25], the evolution of transition metal based compounds has been recognized to terminate with active structure of zero-valent metal[26,27] or stoichiometrically varied compound[28,29]. Nevertheless, the systematic information of catalyst restructuring in whole service life, the evolution law on transition metal's valence state, and the dynamic correlation between space-resolved structure

and time-resolved activity, are lacking. In addition, although the doping strategy has been widely adopted, current knowledge of its working mechanism remains on the adjustment of atomic/electronic structure and defect state. Understanding element-doping affected dynamic reconstruction behavior of catalysts, and the establishment of the structure-activity correlation under various doping conditions, would be essential for the accurate design of efficient catalysts.

Here, in a class of multivalent nickel sulfides, the phase evolution throughout HER process together with valence state evolution, has been revealed via operando characterization techniques, to establish their life-time dynamic structure-activity correlation (Fig. 1). Specifically, pyrite-type NiS_2 shows a spontaneous surface reconstruction into Ni_3S_2 layer with the diffusion and accumulation of sulphur vacancy (V_S), being responsible for catalysis. The reconstruction and subsequent phase transition initiated from surface further propagate into catalyst bulk during the long-term catalytic service. Moreover, partial Fe substitution improves the structure flexibility of NiS_2, which grants more sulphur vacancies to removal and lower the applied potential threshold for phase variation. Such phase reconfiguration enables easier activity triggering and hence optimizes HER performance. The dynamic mechanism of doping strategy as well as the dynamic correlation between space-resolved structure and time-resolved activity have been well investigated. We also demonstrate the universality of figured evolution law for other nickel sulfide catalysts like α-NiS, β-NiS and Ni_3S_4, indicating its potential for expanded multivalent transition metal based catalysts.
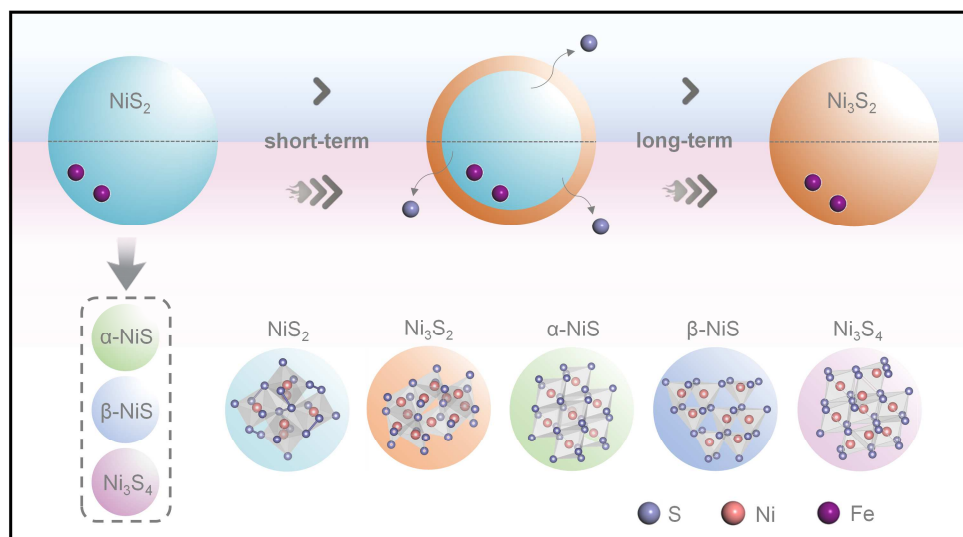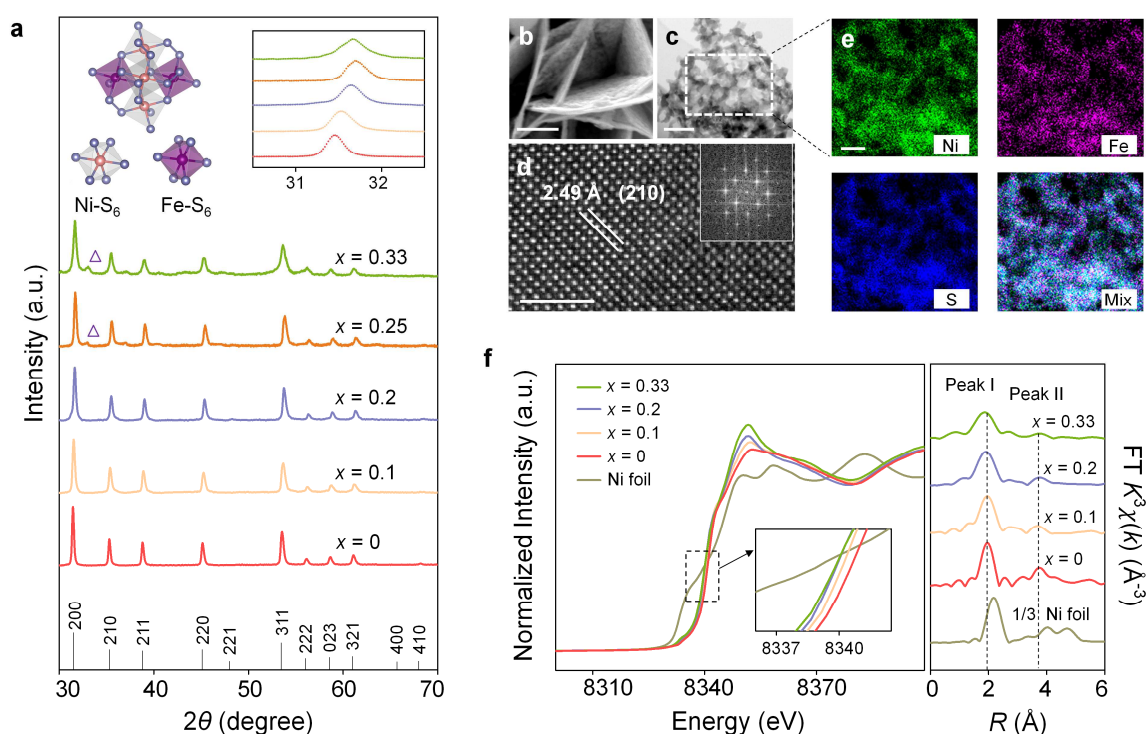
1
2 **Fig. 1 | Schematic illustration of dynamic reconstruction of multivalent nickel sulfide HER catalysts**.
3

4 **Results**

5 **Crystal structure characterization.** The pyrite-type NiS_2 were achieved by annealing as-

6 synthesized α-Ni(OH)$_2$ nanosheets (NSs) (see Supplementary Fig. 1 and Methods for

7 experimental details) with sulphur powder under an argon atmosphere at 400 °C, and the Fe

8 substitution had been well realized with the same method by partially replacing Ni atoms with

9 Fe atoms to form $Ni_{1-x}Fe_x(OH)_2$ NSs ($x \approx 0.1{\sim}0.33$)[30,31]. Such Fe substitution induced electronic

10 interaction plays an important role in modulating the electronic environments of the metal Ni

11 centers, potentially promoting the structural flexibility and the corresponding properties. The

12 detailed characterization results, corroborated by theoretical calculations will be discussed in

13 following sections.

14 The crystal structures of $Ni_{1-x}Fe_xS_2$ ($x \approx 0{\sim}0.33$) NSs were characterized by powder X-ray

15 diffraction (XRD). As displayed in Fig. 2a, the diffraction peaks of as-prepared $Ni_{1-x}Fe_xS_2$

16 match with that of the standard cubic (Pa-3) pyrite-type materials (JCPDS No. 65-3325).

17 Furthermore, the diffraction peak exhibits a shift to a large angle with increasing Fe substitution

18 amount (inset in Fig. 2a), which is ascribed to changes in lattice parameters induced by ionic

5

radius differential between Fe and Ni cations and suggests a solid solution property. Notably,

when $x \geq 0.25$, the diffraction peak appears no more shift, being attributed to the segregation of

FeS_2 (Supplementary Fig. 2). In scanning electron microscopy (SEM) and transmission electron

microscopy (TEM) images (Figs. 2b, c and Supplementary Fig. 3), close-up inspection of

$Ni_{0.8}Fe_{0.2}S_2$ NSs reveals nanosheets structures whose thickness-uniformly distribute between 10

and 20 nm. Also, the high-resolution TEM (HRTEM) image (Fig. 2d) displays clear lattice

fringes with an interplanar spacing of 2.49 Å, indexed to the (210) plane of $Ni_{0.8}Fe_{0.2}S_2$ NSs,

which has been supported by the single-crystal-like diffraction spots from the selected-area

electron diffraction pattern (inset in Fig. 2d). Meanwhile, energy dispersive X-ray spectrum

(EDS) elemental mappings of $Ni_{0.8}Fe_{0.2}S_2$ NSs provide direct-viewing evidence for the uniform

distribution of Ni, Fe and S elements in as prepared nickel sulfides (Fig. 2e).

Fig. 2 | Structural characterizations of as-prepared $Ni_{1-x}Fe_xS_2$ catalysts. **a**, Powder XRD patterns of synthesized $Ni_{1-x}Fe_xS_2$ ($x \approx 0$~0.33) samples. Inset, schematics of the composition of Fe substituted nickel disulfides and the magnified XRD patterns in the range between 30 and 33. The triangle symbols represent diffraction peak of FeS_2 structure. **b**, Top-view SEM image of the $Ni_{0.8}Fe_{0.2}S_2$. Scale bar, 1 μm. **c**, TEM image

of $Ni_{0.8}Fe_{0.2}S_2$. Scale bar, 100 nm. **d**, High-resolution TEM image of $Ni_{0.8}Fe_{0.2}S_2$. Scale bar, 2 nm. The fast Fourier transform is shown in the inset of (**d**) confirms the crystalline nature of the bulk material. **e**, The corresponding EDS elemental mappings of Ni, Fe, S and the mixed elemental mapping. Scale bar, 50 nm. **f**, Normalized Ni K-edge XANES analysis (left axis) of $Ni_{1-x}Fe_xS_2$ samples with Ni foil as reference, as well as the corresponding k^3-weighted Fourier transform (FT) Ni K-edge EXAFS spectra (right axis). Inset, Magnified pre-edge XANES region. Peaks I and II in the FT-EXAFS plots are assigned to Ni-S and Ni-Ni radial distances, respectively.
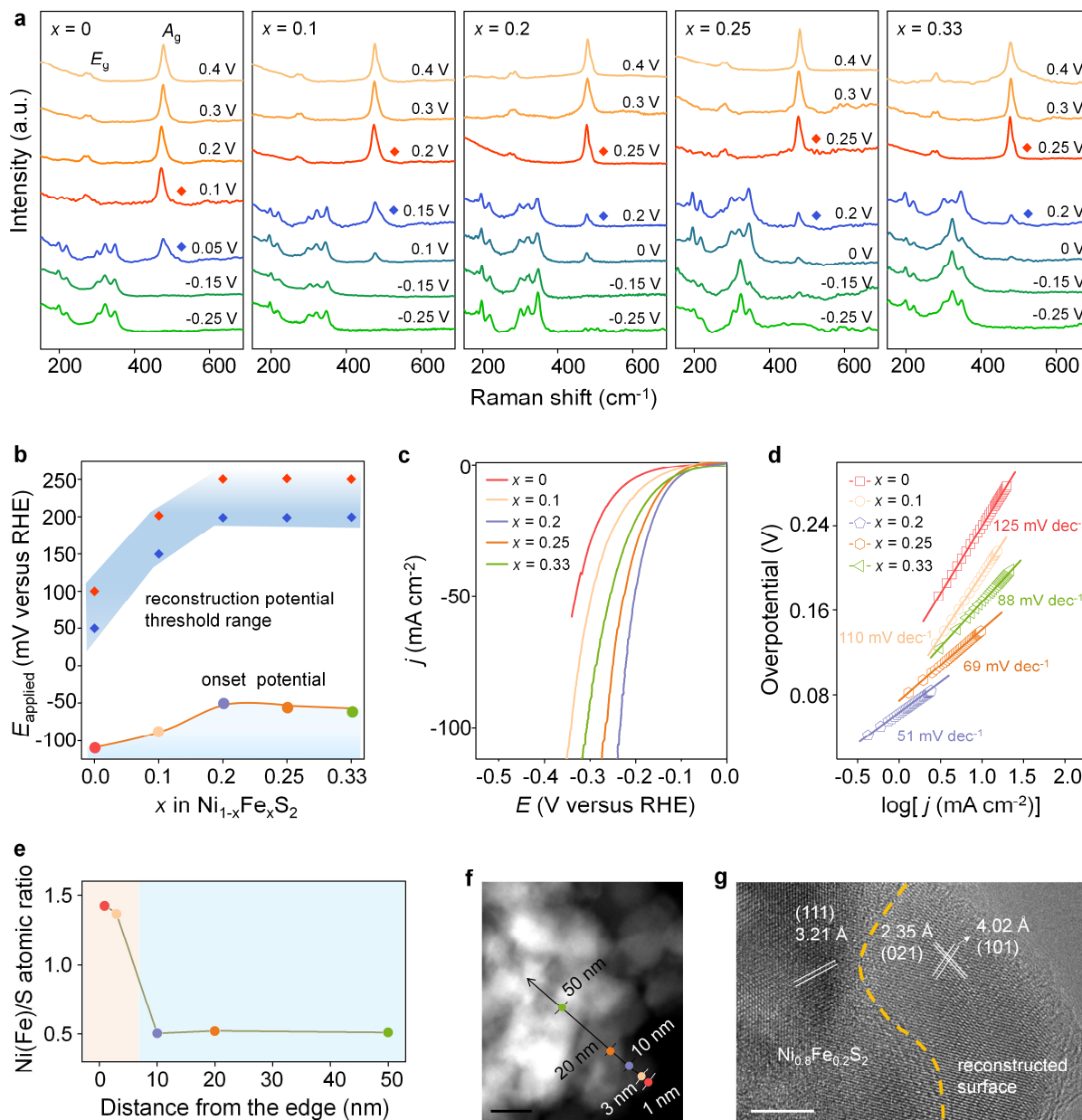
To gain insight into the local electronic and coordination environment of $Ni_{1-x}Fe_xS_2$ ($x \approx$ 0~0.33) NSs, we performed X-ray absorption fine structure (XAFS) measurements at the nickel K edge. X-ray absorption near-edge structure (XANES) results present the Ni absorption-edge shifts to the lower-energy side as the substituted Fe concentration increasing, implying a decrease of Ni valence state in different components (Fig. 2f left axis inset). The K-edge position is determined by the method as described in the references[32-34], and details about edge positions and nominal valence states of Ni and Fe are shown in Supplementary Fig. 4 and Supplementary Table 1. The nominal Ni valence states are supported by the K-edge absorption positions with the calibration of Ni Foil and Ni_2O_3, which are in line with the facts of Ni $2p3/2$ X-ray photoelectron spectroscopy (XPS) peaks shifting to lower binding energies in $Ni_{1-x}Fe_xS_2$ (Supplementary Fig. 5 and Supplementary Table 2). Besides, Fe substitution in NiS_2 also alters the local coordination environment of Ni. As observed from a different perspective in the Fourier transform (FT) Ni K-edge extended X-ray fine structure (EXAFS) analysis in Fig. 2f (right axis), two separate peaks (peaks I and II) at ~1.9 and 3.5 Å are assigned to the features of Ni-S and Ni-Ni bonds. For pyrite-type NiS_2, the unit cell consists of octahedral polyhedron of center nickel atom with six sulphur atoms coordinated (Ni-S_6) motifs. As observed with Ni K-edge EXAFS (Fig. 2f right axis), the first-shell peak I is weakened by Fe substitution, suggesting a lower nickel-sulfide coordination number (CN), more sulphur vacancies, as well

1 as the increased lattice disorder. These results have also been verified by the least-square

2 EXAFS curve-fitting analysis for the first coordination shell of Ni. Specifically, the fitting

3 results of $Ni_{1-x}Fe_xS_2$ ($x \approx 0\sim0.33$) NSs illustrate that Fe substitution reduces the average CN by

4 ~0.6 and the Ni-S bond distance by ~0.4 for $Ni_{0.67}Fe_{0.33}S_2$ (Supplementary Fig. 6 and

5 Supplementary Table 3). Such an effect, indicating an increase in sulphur vacancy, is consistent

6 with the lattice disorder and decreased nickel valence state for Fe doped NiS_2.

7

8 **Phase reconfiguration and dynamic structure-activity correlation.** Nickel sulfides were

9 then investigated by in-situ electrochemical Raman spectroscopy[35-37] to gain an in-depth

10 understanding on the dynamic reconstruction process of surface structures during HER process.

11 According to Raman peaks of pristine pyrite-type NiS_2 and heazlewoodite-type Ni_3S_2 from

12 Supplementary Fig. 7 and Supplementary Table 4, the corresponding characteristic peaks in Fig.

13 3a have been identified[38-40]. For the in-situ Raman measurement of NiS_2 ($x = 0$), as the applied

14 potential increases cathodically from 0.4 to -0.25 V (more negative versus the reversible

15 hydrogen electrode, vs. RHE), the characteristic peaks assigned to NiS_2 gradually decay till

16 disappear along with the emerging and progressive growth of Ni_3S_2 peaks. This is interpreted

17 that NiS_2 undergoes a spontaneous phase evolution process whose reconstruction potential

18 threshold locates between 0.1 to 0.05 V (vs. RHE). One observation of note is the continuous

19 redshift of A_g and E_g peaks of NiS_2 with applied potentials varied from 0.4 to 0.1 V vs. RHE

20 (Supplementary Fig. 8 and Supplementary Table 5). Such phenomenon suggests the softening

21 of S-S bonds, which could be attributed to the generation and the subsequent accumulation of

22 sulphur vacancy before the above mentioned activation of qualitative surface reconstruction [41].

In term of a series of $Ni_{1-x}Fe_xS_2$ samples ($x = 0.1, 0.2, 0.25, 0.33$), the similar quantitative change of sulphur vacancy accumulation and the following qualitative change of phase transition processes have been well illustrated (Fig. 3a). Also, the quantitative changing rate and the qualitative changing threshold accordingly vary with the Fe doping amount. That is to say, with the incremental Fe doping in Fig. 3b, the reconstruction potential threshold range gradually moves to the positive direction. However, it basically remains unchanged between 0.25~0.2 V (vs. RHE) when $x > 0.2$, indicating the dominated position of the low Fe substitution levels towards the reconstruction potential threshold of nickel sulfides.

Fig. 3 | In-situ investigation of dynamic surface reconstruction process and HER performances of catalysts. a, In-situ Raman spectra of $Ni_{1-x}Fe_xS_2$ ($x \approx 0\sim0.33$) samples at the potentials of 0.4~-0.25 V versus reversible hydrogen electrode (vs. RHE) in 1M KOH. **b**, The surface reconstruction potential threshold range for $Ni_{1-x}Fe_xS_2$ ($x \approx 0\sim0.33$) samples, and the corresponding onset potentials of hydrogen evolution are plotted to show the dynamic correlation of structure-activity. The red diamond dots represent the final potential of existence for Raman peaks of $Ni_{1-x}Fe_xS_2$ structures, and the blue diamond dots stand for the potential of emerging of Ni_3S_2 Raman peaks. **c**, HER polarization curves of $Ni_{1-x}Fe_xS_2$ catalysts on carbon fiber paper in N_2-saturated 1M KOH at a scan rate of 5 mV s^{-1}, **d**, Corresponding HER Tafel plots derived from the polarization curves. **e, f**, Elemental composition of post-electrolysis $Ni_{0.8}Fe_{0.2}S_2$ determined from EDS at a series of spots along a line from the crystallite edge to the bulk reveals the variation in Ni(Fe):S composition across the crystallite, the marked points in (**f**) denote the scanning distance along the pathway in nm. **g**, HRTEM image of post-electrolysis $Ni_{0.8}Fe_{0.2}S_2$. The scale bars are 20 nm in (**f**), 5 nm in (**g**).
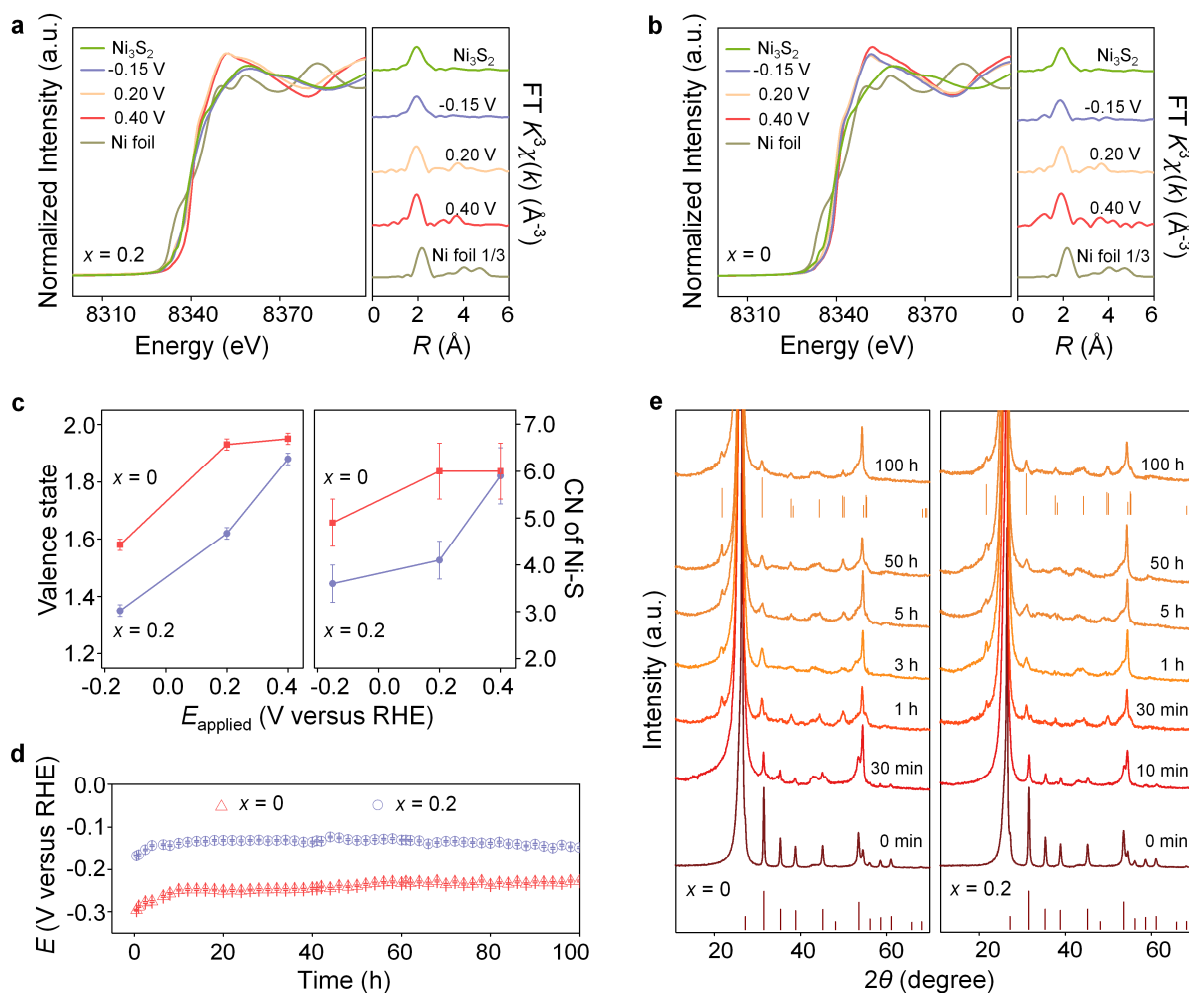
The electrochemical HER activity of $Ni_{1-x}Fe_xS_2$ NSs have been systematically investigated under alkaline conditions (for detail see Methods). The steady-state linear sweep voltammetry (LSV) in N_2-saturated 1 M KOH, as shown in Fig. 3c, demonstrates that NiS_2 exhibits an overpotential of 233 mV at the current density of 10 mA cm^{-2}. As the Fe doping amount x increases before reaching 0.2, the corresponding overpotential @10 mA cm^{-2} continues to decrease to 122 mV, and then it bounces back beyond 0.2 (Supplementary Fig. 9a). The Tafel slope, as a pivotal kinetic parameter, is usually used to investigate the rate determining step of an electrochemical process. Here, compared with 125 mV dec^{-1} for NiS_2, $Ni_{0.8}Fe_{0.2}S_2$ ($x = 0.2$) performs superior properties over other Fe-doped catalysts, with the Tafel slope as low as 51 mV dec^{-1}, as shown in Fig. 3d, suggesting the Volmer–Heyrovsky mechanism as the HER pathway[42,43]. The activity differencial of nickel sulfides is in accordance with the electrochemical impedance spectroscopy results and the double-layer capacitance plot data. As shown in Supplementary Fig. 9b, Nyquist plots are fitted to a simplified Randles equivalent circuit model[44], and the charge-transfer resistance (R_{ct}) of $Ni_{1-x}Fe_xS_2$ measured at 200 mV overpotential decline considerably in comparison with that of NiS_2 (R_{ct} is 14 Ω), and $Ni_{0.8}Fe_{0.2}S_2$ shows the smallest R_{ct} value of 6.5 Ω. These results demonstrate that an appropriate Fe doping concentration extraordinarily promotes the charge transfer, thus both improving the reaction efficiency and propelling efficient electrical integration to reduce parasitical ohmic loss. The double-layer capacitance (C_{dl}) scales roughly with the effective electrochemically active surface area[45], and its value can be estimated from the slope of the linear relationship between the half capacitive current density ((j_{anodic} - $j_{cathodic}$)/2) at the middle of the applied potential range and the scan rates in Supplementary Fig. 10. Significantly, our results reveal a

1 considerably larger C_{dl} of $Ni_{0.8}Fe_{0.2}S_2$ (67 mF cm^{-2}) compared with NiS_2 (4 mF cm^{-2}),

2 suggesting more accessible active sites created on $Ni_{0.8}Fe_{0.2}S_2$ catalyst.

3 According to the LSV curve of the catalytic performance measurement, the relationship

4 between the HER onset potentials (@ 0.5 mA cm^{-2}) and the Fe doping amount has also been

5 plotted in Fig. 3b. The exhibited synchronous trend between reconstruction potential threshold

6 range and onset potential when $x \leq 0.2$ implicates the close correlation concerning

7 reconstruction initiate and HER activation, further implicating the resulted Ni_3S_2 phase at the

8 surface should be responsible for the HER activity. Specifically, the reconstruction potential

9 threshold of $Ni_{0.8}Fe_{0.2}S_2$ locates between 0.25~0.2 V (vs. RHE) while it moves into the range

10 between 0.1~0.05 V (vs. RHE) for pristine NiS_2. Such shift apparently verifies that appropriate

11 Fe substitution is beneficial for reducing necessary energy consumption to ignite the phase

12 reconfiguration process. It is attributed to the varied sulphur vacancy concentration in as-

13 prepared $Ni_{1-x}Fe_xS_2$ catalysts, indicated from XAFS results in Fig. 2f. When with Fe substitution

14 in NiS_2 structures, more sulphur vacancies grant the facile removal of the sulphur atoms from

15 the surface, and at the same time enable the interdiffusion of the component atoms under

16 working conditions[13]. Correspondingly, the onset potential of $Ni_{0.8}Fe_{0.2}S_2$ declines by about 50

17 mV as comparison with NiS_2. The cyclic voltammetry (CV) curves in Supplementary Fig. 11

18 also suggest consistent results. The reduction peak in the first cycle appears at ~0.1 V (vs. RHE)

19 for $Ni_{0.8}Fe_{0.2}S_2$, while an obvious negative peak shift is observed for NiS_2 (~0.0 V vs. RHE),

20 which suggest that Fe substitution facilitates the pre-reduction of Ni as well as subsequent

21 surface reconstruction initiate.

22 In addition, the irreversible morphology change on catalyst surface during HER

measurement was monitored (Figs. 3 e, f, g and Supplementary Fig. 12). The catalysts sprayed on Cu grids, which were attached to Au electrode with conductive carbon tape, have been polarized in N_2 saturated 0.01 M NaPi electrolyte (sodium phosphate, pH 7.2) at -0.45 V (vs. RHE) for 2 h. EDS results display that the Ni(Fe):S atomic ratio is 1.43:1.0 at the edge of the nanosheet, and this ratio rapidly increases to 1.0:2.0 as the scan proceeds to the interior, reflecting the bulk stoichiometry. Also, the 5 nm thick reconstructed phase shell, indexed to the (101) and (021) planes of Ni_3S_2, were observed on the surface of bulk $Ni_{0.8}Fe_{0.2}S_2$ catalyst. These visualization results again support the undergoing reconstruction of pre-catalyst.

Fig. 4 | Operando XAFS spectra and long-term operation characterization of catalysts. a, b, Normalized operando Ni K-edge XANES analysis (left axis) at 0.40, 0.20, and -0.15 V (vs. RHE) with Ni Foil and standard Ni_3S_2 powder (Alfa Aesar) as reference, as well as the corresponding operando FT k^3-weighted Ni

K-edge EXAFS (right axis): $Ni_{0.8}Fe_{0.2}S_2$ (**a**) and NiS_2 (**b**). **c**, Left axis, the fitted average valence states of nickel element from XANES spectra for NiS_2 and $Ni_{0.8}Fe_{0.2}S_2$. Error bars represent the standard deviation from at least three independent measurements. The right axis show the changes of coordination number (CN) for Ni-S corresponding to the applied potentials. **d**, Chronopotentiometric curves obtained with $Ni_{0.8}Fe_{0.2}S_2$ and NiS_2 at constant current density of 10 mA cm^{-2}. **e**, XRD patterns of catalysts after the operation of HER instantly at 10 mA cm^{-2} during 100 h. The 2θ peaks of ~26.5° and 54.5° stand for the carbon fiber paper substrates.

Thereafter, attention was directed to the dynamic evolution of electronic structure and local coordination environment via operando XAFS for as-prepared nickel sulfides during the practical electrochemical reaction. Figs. 4a, b illustrate the operando XANES and the FT-EXAFS spectra in R-space of $Ni_{0.8}Fe_{0.2}S_2$ and NiS_2 recorded at 0.4 V, 0.2 V and -0.15 V (vs. RHE). Note that in left axis of Figs. 4a and b, absorption K-edges of both samples gradually shift to a lower energy position with the potential increase cathodically during HER process. This clearly explains the reduced valence state of nickel, which is attributed to the reconstruction in nickel sites. The corresponding nominal valence states of Ni in both samples under each applied potential are shown in Fig. 4c left based on the results from Supplementary Fig. 4. The average valence state of Ni in $Ni_{0.8}Fe_{0.2}S_2$ at 0.40 V (vs. RHE) is approximately +1.88, and it decreases to +1.62 and +1.35 at 0.20 and -0.15 V (vs. RHE), respectively. While for NiS_2, the average valence state has a negligible decrease at 0.20 V compared with 0.4 V (vs. RHE), and it reaches +1.58 at -0.15 V (vs. RHE). This demonstrates the promotion effect on Ni reduction originated from Fe substitution, which is in accord with the results of phase transition and effectively supports the rational inference regarding its contribution on reconfiguration process.

In the case of local coordination environment, similar results are acquired from the FT-EXAFS spectra in R-space (right axis of Figs. 4a, b). Compared with the profiles collected at

0.4 V vs. RHE, the Ni-S bond peak in both samples decrease at -0.15 V vs. RHE, indicating Ni

atom accumulation in Ni-S$_4$ tetrahedral coordination resulted from reconstruction. More

precisely for fitting results (right axis in Fig. 4c), the Ni-S CN decreases to 4.1 ± 0.4 and $3.5 \pm$

0.4 for Ni$_{0.8}$Fe$_{0.2}$S$_2$ at 0.20 and -0.15 V vs. RHE from 5.9 ± 0.6 at 0.4 V vs. RHE. While for

NiS$_2$, the decline trend is obviously delayed (Supplementary Figs. 13, 14 and Supplementary

Table 3). Notably, the absorption edge and CN of Ni$_{0.8}$Fe$_{0.2}$S$_2$ at -0.15 V (vs. RHE) is closer to

that of standard Ni$_3$S$_2$ sample (the average valence state of Ni in standard Ni$_3$S$_2$ is about +1.20,

in Supplementary Fig. 15), further verifying a more thorough reconstruction process with the

distorted Ni tetrahedral structure enabled by Fe doping.

The lower tendency of both Ni valence state and CN in the cathodic process on nickel sulfides

surface could be viewed as a desulphurization process, and the delayed Ni reduction for pristine

NiS$_2$ suggests a relatively limited desulphurization process. This elucidates that Fe substitution

activate the structure to facilitate quantitative accumulation of sulphur vacancy and the

interdiffusion of component atoms, as well to subsequently germinate the phase transition with

unsaturated nickel-sulphur sites, reconfirming that the phase evolution together with the lower

valence state evolution tendency are strongly correlated with the sulphur atom behavior.

Therefore, the surface of pyrite-type nickel sulfide catalyst is inclined to reconstruct soon

after desulphurization, to generate the Ni$_3$S$_2$ structure. Such critical process, consisting of the

quantitative (sulphur vacancy accumulation) to qualitative alternation (phase transition), is

effectively facilitated by introduction of proper sulphur vacancy, to empower the catalytic HER

activity easier to be triggered. To sum up, the phase reconfiguration process, indicated by the

evolution law of phase transition and valence state, is dominated by Fe doping with a sulphur

1   vacancy mediated mechanism.

2   In order to investigate the long-term structure-activity correlation at catalyst during the whole

3   HER service life, the stability test for the nickel sulfide/carbon fiber paper electrodes at a fixed

4   current density of 10 mA cm^{-2} was conducted. As shown in Fig. 4d, the exhibited negligible

5   activity decay even over 100 h demonstrates their superior stability under the alkaline

6   environment. To follow the phase transition from their as-synthesized pre-state into the

7   practically true state of the whole catalyst, XRD analysis was employed (Fig. 4e). The

8   diffraction peaks of NiS_2 gradually fade away with Ni_3S_2 peaks emerging to finally reach a total

9   phase transition throughout the electrolysis duration, demonstrating the terminated stable phase

10   of Ni_3S_2. Simultaneously considering in-situ Raman results, as well as the corresponding

11   surface chemical states of Ni probed by the XPS data during the long-term operation are

12   provided in Supplementary Fig. 16 and Supplementary Table 2, it is confirmed that the phase

13   transition initially starts from the catalyst surface and subsequently extends to the bulk structure.

14   The life-time dynamic structure-activity correlation during HER service of nickel-based sulfide

15   compounds is further established by comprehensively considering the transient reconstruction

16   triggered activity and the long-term bulk phase transition maintained stability.

17

18   **Dynamic mechanism of phase reconfiguration**. To further validate the dominant sulphur

19   vacancy as inner driving force for phase reconfiguration and the effective tuning capability of

20   proper Fe substitution, density functional theory (DFT) calculations were conducted. The

21   computational models for $Ni_{1-x}Fe_xS_2$ ($x = 0$ and 0.2) are presented in Fig. 5a. The projected

22   density of state (PDOS) of $Ni_{1-x}Fe_xS_2$ and their band center energies are given in Fig. 5b (for

more details see Supplementary Table 6). When Fe is substituted in NiS_2, S $3p$ band center energy is raised to be closer to the Fermi level, allowing for the reduction of energy penalty to create sulphur vacancy, which is beneficial for the formation of sulphur vacancy in nickel sulfide[46]. Similar inference is reached based on lower sulphur vacancy formation enthalpy (0.75 eV for $Ni_{0.8}Fe_{0.2}S_2$ and 0.86 eV for NiS_2) from Fig. 5c and details in Supplementary Tables 1 and 7, thus resulting in the highest sulphur vacancy concentration (δ) approximate 0.13 with 0.2 Fe substitution. The catalyst structural flexibility, enabled by initial high anion vacancy concentration, is believed to be capable of accommodating even more anion vacancies during the electrocatalysis[21, 22]. This capacitates the easy migrating and leaching of sulphur atoms from nickel sulfide surface, while simultaneously aiding interdiffusion of the constituent atoms, via the sulphur vacancy mediated mechanism under operation condition.
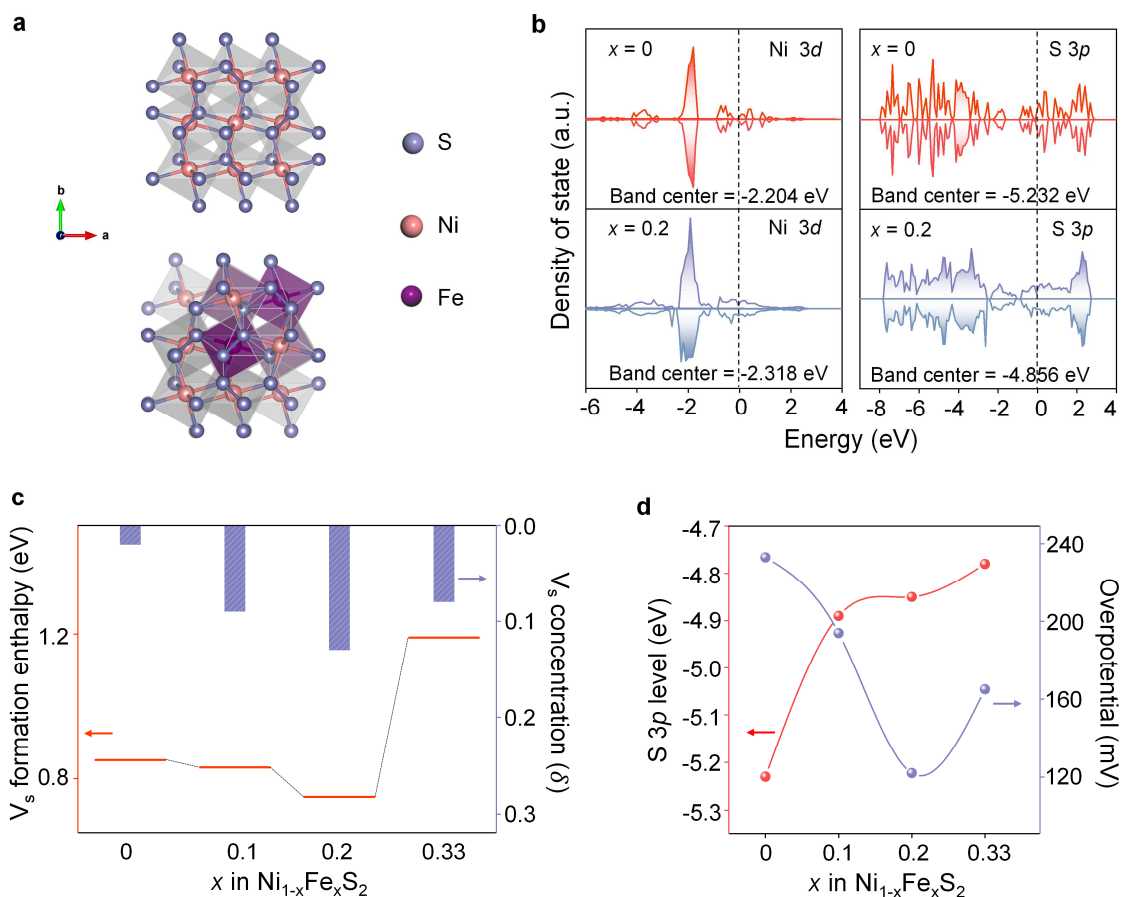
Fig. 5 | Electronic interpretation of the effect of Fe substitution on catalyst evolution. a, Computational models of $Ni_{1-x}Fe_xS_2$: top, $x = 0$; bottom, $x = 0.2$. **b**, Computed Ni $3d$, S $3p$ PDOS of $Ni_{1-x}Fe_xS_2$ ($x = 0.0, 0.2$). **c**, Calculated sulphur vacancy (V_S) formation enthalpy and sulphur vacancy concentration (δ) of the samples for $Ni_{1-x}Fe_xS_2$ ($x = 0.0, 0.1, 0.2, 0.33$). **d**, Computed S $3p$ PDOS related to the overpotential of $Ni_{1-x}Fe_xS_2$ ($x = 0.0, 0.1, 0.2, 0.33$) @ 10 mA cm^{-2}.

Furthermore, as the Ni $3d$ band expands gradually with the incremental Fe substitution amount, its overlap with the S $3p$ band becomes larger, verifying the enhanced Ni-S covalency due to the increased hybridization between Ni $3d$ and S $3p$ orbital. In Supplementary Table 6, when x ranges from 0 to 0.33, the Ni $3d$-S $3p$ exhibits an obvious diminishment, indicating that the Ni $3d$-S $3p$ hybridization is enhanced by increasing Fe substitution amount. This benefits the sulphur redox reaction and the mutual diffusion when a cathodic potential is applied. The sulphur atom in the lattice is easier to be leached to create more sulphur vacancies to subsequently boost the qualitative phase transition. This trend is in consistent with the HER

activity in terms of overpotential when $x \leq 0.2$ in Fig. 5d. However, as for $x = 0.33$, its overpotential unexpectedly rises, which originated from the inhibition of further sulphur vacancy creating with excessive Fe-S bonds. This phenomenon is also explained by the increased enthalpy of sulphur vacancy formation in Fig. 5c. Additionally, the calculated formation energy differential for reconstruction (Supplementary Table 8) again confirms the superiorities of Fe substitution towards phase reconfiguration.

Combining theory and experiments, the quantitative accumulation of sulphur vacancy induced catalyst structure flexibility has been identified as the origin for the accelerated qualitative phase transition during catalytic electrolysis. Notably, this also reveals a dynamic mechanism of doping strategy that influences the phase reconfiguration process via tuning anion behavior as a bridge.

Universality of catalyst evolution. Besides NiS_2, the above demonstrated phase evolution to Ni_3S_2 has been extended to α-NiS, β-NiS and Ni_3S_4 HER catalysts. Their crystal structure and local chemical state characterization results are illustrated in Supplementary Fig. 17 and Supplementary Tables 2, 4. According to the in-situ Raman data from Fig. 6a and Supplementary Table 9, their reconstruction potential thresholds locate in varied regions of 0.1~0.05 V, 0.15~0.1 V and 0.1~0.05 V (vs. RHE), respectively, illustrating different energy barriers to overcome during reconstruction. And this is consistent with corresponding reduction peaks in the cycles for restructuring process at surface (Fig. 6b). Comparatively, the reduction peak in the first cycle appears at ~0.03 V (vs. RHE) for β-NiS, while negative shifts are observed for α-NiS and Ni_3S_4. Considering about 50 mV lower restructuring potential for β-NiS, it could

be speculated that its lower CN of Ni-S_5 motif is responsible for easier transition to the Ni-S_4 motif of Ni_3S_2[6]. The overpotential (@ 10 mA cm^{-2}, η_{10}) of β-NiS is about 70 mV and 20 mV lower compared with α-NiS and Ni_3S_4, respectively. Such correlation between the reconstruction potential threshold differential and HER performance variation signalizes the dominance of phase evolution during HER catalytic reaction.

Fig. 6 | Dynamic structural evolution characterization of α-NiS, β-NiS and Ni_3S_4 catalysts. a, In-situ Raman spectra of nickel sulfides at the potentials of 0.4~-0.25 V (vs. RHE) in 1M KOH for α-NiS, β-NiS and Ni_3S_4. **b**, Cyclic voltammetry curves of α-NiS, β-NiS and Ni_3S_4 in N_2-saturated 1 M KOH with a scan rate of 2 mV s^{-1} between 0.4 and -0.4 V (vs. RHE). The red diamond dots represent the final potential of existence for α-NiS, β-NiS and Ni_3S_4 Raman peaks, and the blue diamond dots stand for the potential of emerging of Ni_3S_2 Raman peaks. **c**, XRD patterns of catalysts after the operation of HER instantly at constant current density of 10 mA cm^{-2}.

For XRD patterns during the long-term service in Fig. 6c, the intensity of Ni_3S_2 peaks rise slightly along with the gradual disappearance of β-NiS peaks for the first hour. And the bulk phase transformation was realized basically after 5h electrolysis. Similar for α-NiS and Ni_3S_4, the terminated bulk phases are both confirmed as Ni_3S_2. In short, nickel sulfides including NiS_2,

20

α-NiS, β-NiS and Ni_3S_4 are all demonstrated to perform phase evolution process with unified and terminated Ni_3S_2 structure. These results indicate the electrochemical universality of structural evolution for nickel sulfide catalysts, and figure a lower valence state evolution tendency of nickel in the catalytically terminated phase of HER, which implicates a general phenomenon during the restructuring of multivalent transition metal based catalysts.

Conclusions

In summary, the spontaneous phase evolution phenomena as well as the dynamic structure-activity correlations for the whole service life of a class of multivalent nickel sulfides during their HER service have been investigated from multiple dimensions including variations of phase, valence state and coordination environment via operando electrochemical spectroscopy techniques. The diffused and accumulated sulphur vacancies on nickel sulfide catalyst lead to surface reconstruction and phase transition with terminated Ni_3S_2 structure responsible for subsequent catalysis. Such quantitative to qualitative alternation is prompted with Fe doping which enables the structural flexibility to accommodate more sulphur vacancies for the phase reconfiguration, and hence improves HER performance at an optimal dopant amount of 20%. Based on this, we also established the dynamic mechanism of doping strategy, which is widely adopted for promoting catalytic activity but has only been understood in the static level. Beyond propagation from surface into bulk after prolonged service, the phase evolution has also been universally confirmed from NiS_2 to α-NiS, β-NiS and Ni_3S_4. The findings indicate a general law of lower valence state evolution tendency along with the phase evolution of multivalent transition metal catalyst under HER condition, evidence a fundamental idea that the dynamic

1 evolution of catalysts dominates the finalized catalytic activity, and provide an alternative

2 strategy of phase reconfiguration for developing superior catalysts.

3

4 **Methods**

5 **Material synthesis.** $Ni_{1-x}Fe_xS_2$ (x = 0, 0.1, 0.2, 0.25, 0.33) powders were prepared by a typical

6 procedure. In a first step, nickel (II) nitrate hexahydrate ($Ni(NO_3)_2 \cdot 6H_2O$, Sigma-Aldrich,

7 98.5%) and iron(II) sulfate heptahydrate ($FeSO_4 \cdot 7H_2O$, Sinopharm Chemical Reagent Co., Ltd,

8 99%) in specific molar ratio were dissolved in deionized water, followed by the addition of urea

9 (Aladdin, 99%) and ammonium fluoride (Aladdin, 98%). After stirred for 30 min, the

10 suspension was transferred to a 50 mL Teflon-lined stainless-steel autoclave and heated at 120 ℃

11 for 10 h before cooling to room temperature. The resultant precipitate was centrifuged and

12 washed by deionized water and ethanol and dried at 60 ℃ for 1 h. The as prepared $NiFeO_xH_y$

13 LDH was sufficiently mixed with sulphur powder (Alfa Aesar, ~100 mesh, 99.5%, 1:5) by

14 grinding for 30 min. The mixture was then placed in the center of a quartz tube in an aluminum

15 oxide boat, and heated at 400 ℃ for 1 h in an argon atmosphere to obtain pyrite $Ni_{1-x}Fe_xS_2$.

16 Finally, the obtained compounds were ultrasonicated, washed several times and dried under

17 vacuum overnight. For the Ni_3S_4 and β-NiS, the hydrothermal method was used in the solution

18 of carbon disulfide (CS_2, Aladdin, 99%) and sodium sulfide nonahydrate ($Na_2S \cdot 9H_2O$, Aladdin,

19 98%) in a 50 mL Teflon-lined stainless-steel autoclave at 200 ℃ for 10 h with $NiCl_2 \cdot 6H_2O$ and

20 $Ni(OH)_2$ LDH, respectively. α-NiS was obtained using thiourea (($NH_2)_2CS$, Alfa Aesar, 98.5%)

21 and $NiCl_2 \cdot 6H_2O$ (Aladdin, 98%) in a 50 mL Teflon-lined stainless-steel autoclave filled with

22 hydrazine hydrate ($N_2H_4 \cdot H_2O$, 50 wt.% content, J&K) at 120 ℃ for 24 h. The nickel sulfides

1 on carbon fiber paper (CFP, TORAY, thickness of 0.18 mm) were also prepared through the

2 above method just adding CFP in the solution.

3

4 **Characterizations**. The XRD patterns of bulk nickel sulfides were recorded on a Rigaku TTR3

5 diffractometer at a scanning rate of 2° min^{-1}, using Cu-Kα radiation (λ = 1.5418 Å). XPS data

6 were obtained using an ESCALab250 electron spectrometer from Thermo Fisher Scientific

7 Corporation with monochromatic 150 W AlKα radiation. Pass energy for the narrow scan is 30

8 eV. The base pressure was about 6.5×10^{-10} mbar. The binding energies were referenced to the

9 C1s line at 284.8 eV from alkyl or adventurous carbon.

10 The nickel sulfide morphologies were characterized by SEM (FEI Quanta 3D) at an

11 accelerating voltage of 5 kV. The crystal structures and detailed information about the

12 morphologies and element compositions were obtained using TEM (JEM-120F) and the energy

13 dispersive X-ray spectroscopy (EDS) (JEOL JED-2300 Analysis Station) with an accelerating

14 voltage of 200 kV. The nickel sulfide catalysts samples were drop cast onto Cu TEM grids and

15 then attached to the Au electrode with conductive carbon tape polarized in N_2 saturated 0.01 M

16 NaPi electrolyte, pH 7.2. The treated samples were rinsed with reagent grade water, dried in a

17 stream of N_2. The EDS scans were collected at various positions in the sample extending from

18 the surface layer to the interior of the samples.

19

20 **Electrochemical measurements.** All electrochemical measurements were carried out in a

21 typical three-electrode system with an electrochemical workstation (CHI 660E, Shanghai

22 Chenhua, China) at room temperature, and using a platinum plate as the counter electrode and

saturated Ag/AgCl as the reference electrode. The prepared Ni-based sulfide/CFP (0.5 cm^2)

used as the working electrode. For HER, cathodic linear sweep voltammetry with a 5 mV s^{-1}

scan rate was performed in N_2-saturated 1.0 M KOH (pH 13.6, Aladdin, 95%). Electrochemical

impedance spectroscopy measurements were carried out by applying an a.c. voltage with 10

mV amplitude in a frequency range from 100 kHz to 10 mHz at an overpotential of 200 mV.

All potentials were calibrated versus RHE using

$$E \text{ (RHE)} = E \text{ (Ag/AgCl)} + 0.197 \text{ V} + 0.0592 \times \text{pH}$$

For all polarization curves presented in the paper, the iR values were manually corrected with

the series resistance (R_s) on the basis of the equation:

$$E \text{ (RHE)} = E \text{ (Ag/AgCl)} + 0.197 \text{ V} + 0.0592 \times \text{pH} - iR_s$$

The compensated ohmic R_s values were obtained from the fittings of electrochemical impedance

spectra.

In-situ Raman spectroscopy. Raman spectroscopy was carried out with a Horiba Jobin-Yvon

Labram HR 800 Micro-Raman instrument and Labspec software. All Raman spectra were

acquired with 532 nm excitation from a 250 mW diode laser. The incident laser power was

decreased by a factor of 100 to avoid sample damage. A 50 × magnification long working

distance (8 mm) objective was used. Raman frequencies were calibrated using Si wafer (520.7

cm^{-1}). The measurements of in-situ Raman spectra were carried out in a home-built cell

(Supplementary Fig. 18) filled with 1 M KOH electrolyte, with Ag/AgCl and platinum foil as

reference and counter electrodes, respectively. Acquisition of spectra at steady-state conditions

was performed after holding the catalyst at the desired potential for 5 min. To prepare the

1 working electrode, 4 mg electrocatalyst and 20 µl Nafion solution (5 wt%, Sigma-Aldrich) were

2 ultrasonically dispersed in 1 ml water/ethanol (vol/vol = 3:1) solution to form a homogeneous

3 ink. The electrocatalyst suspension (10 µl) was loaded onto glass carbon (3 mm) as the working

4 electrode.

5

6 **Operando X-ray absorption measurements.** The Ni K-edge (8333 eV) XAFS spectra were

7 measured at the 1W2B beamline of Beijing Synchrotron Radiation Facility (BSRF), China. The

8 storage ring of BSRF was operated at 2.5 GeV with a maximum electron current of 250 mA.

9 Operando XAFS measurements were performed with catalyst-coated carbon paper using a

10 home-built cell (Supplementary Fig. 19). The catalyst was spray onto carbon paper taped with

11 Kapton film on the back as the working electrode (~1 cm × 1 cm) to ensure all of the

12 electrocatalyst reacted with KOH electrolyte at a geometric metal loading of ~1 mg cm^{-2}. The

13 operando XAFS spectra were collected through the fluorescence mode to monitor the changes

14 during the HER process, cathodic voltages at 0.40, 0.20 and -0.15 V (vs. RHE) were applied

15 for 5 min in 1 M KOH as the conditioning step.

16 During XAFS measurements, we calibrated the position of the absorption edge (E_0) using Ni

17 foil, and all the XAFS data were collected during one period of beam time. The standard

18 samples of Ni foil, Ni_3S_2 (Alfa Aesar, 99.9%) and Ni_2O_3 (Macklin, 99.5%) were measured in

19 the transmission mode. The position of E_0 is defined as the point corresponding to the maximum

20 value in the derivative curves of the XANES spectra. The obtained XAFS data was processed

21 in Athena (version 0.9.25) for background, pre-edge line and post-edge line calibrations. Then

22 Fourier transformed fitting was carried out in Artemis (version 0.9.25)[47]. The k^3 weighting, k-

1 range of 3~11 Å^{-1} and R range of 1~3 Å were used for the fitting. The model of bulk Ni, NiS_2,

2 NiS and Ni_3S_2 were used to calculate the simulated scattering paths. The four parameters,

3 coordination number, bond length, Debye-Waller factor and E_0 shift (CN, R, σ^2, ΔE_0) were fitted

4 without anyone was fixed, constrained, or correlated.

5

6 **DFT calculations.** The ab initio simulations mentioned in this work that related to density

7 functional theory (DFT) was conducted using the Vienna ab initio simulation package (VASP)[48].

8 Projector augmented wave (PAW) potentials was chosen to treat ion-electron interactions, and

9 the exchange-correlation contributions were approximated by the generalized gradient

10 approximation (GGA) method, the Perdew–Burke–Ernzerhof (PBE) functional[49]. In the process

11 of optimizing lattice structure of NiS_2, conjugate gradient algorithm with a force tolerance of

12 0.01 eV/Å and a kinetic energy cutoff 500 eV was as convergence criteria. The Gamma k-point

13 sampling was set to be 9 × 9 × 9 for materials. The optimized NiS_2 crystalline cell was built

14 into supercell along (111) direction and Fe doped NiS_2 models were achieved by replacing Ni

15 atoms with Fe atoms randomly in NiS_2 supercell model. For these supercells, the k-point mesh

16 was set as 5 × 5 × 1, and all the other simulation parameters remain unchanged in the self-

17 consistent calculations. The vacancy formation energy was calculated by the equation of

18 $E_{\text{vacancy\_formation}} = E_{\text{S\_defect}} - (E_{\text{perfect}} - E_{\text{S\_element}})$, E_{perfect} is the total energy of perfect NiS_2, $E_{\text{S\_defect}}$

19 is the total energy of NiS_2 with sulphur vacancy, $E_{\text{S\_element}}$ is the averaged total energy for each

20 sulphur atom in its most stale elemental form (i.e. Rhombic sulphur).

21

22 **Data Availability**

The data supporting the findings of this study are available within this article and its Supplementary Information, or from the corresponding author upon reasonable request.

References

1. Turner, J. A. A realizable renewable energy future. *Science* **285**, 687–689 (1999).

2. Gasteiger, H. A. & Marković, N. M. Just a dream—or future reality? *Science* **324**, 48-49 (2009).

3. Seh, Z. W. et al. Combining theory and experiment in electrocatalysis: Insights into materials design. *Science* **355**, eaad4998 (2017).

4. Chu, S., Cui, Y. & Liu, N. The path towards sustainable energy. *Nat. Mater.* **16**, 16-22 (2017).

5. Hansen, T. W. et al. Atomic-resolution in situ transmission electron microscopy of a promoter of a heterogeneous catalyst. *Science* **294**, 1508-1510 (2001).

6. Yan, B. et al. Surface restructuring of nickel sulfide generates optimally coordinated active sites for oxygen reduction catalysis. *Joul* **1**, 600-612 (2017).

7. Tian, X. et al. Engineering bunched Pt-Ni alloy nanocages for efficient oxygen reduction in practical fuel cells. *Science* **366**, 850–856 (2019).

8. Nong, H. N. et al. A unique oxygen ligand environment facilitates water oxidation in hole-doped IrNiOx core–shell electrocatalysts. *Nat. Catal.* **1**, 841–851 (2018).

9. Shi, Y., Yu, Y., Liang, Y., Du, Y. & Zhang, B. In situ electrochemical conversion of ultrathin Tannin-NiFe complex film as an efficient oxygen-evolving electrocatalyst. *Angew. Chem. Int. Ed.* **58**, 3769-3773 (2019).

10. Cao, L. et al. Identification of single-atom active sites in carbon-based cobalt catalysts during electrocatalytic hydrogen evolution. *Nat. Catal.* **2**, 134-141 (2019).

11. Li, S. et al. Operando revealing dynamic reconstruction of NiCo carbonate hydroxide for high-rate energy storage. *Joule* **4**, 1–15 (2020).

12. Sun, D. et al. Ordered intermetallic Pd_3Bi prepared by an electrochemically induced phase transformation for oxygen reduction electrocatalysis. *ACS Nano* **13**, 10818−10825 (2019).

13. Wang, D. et al. Spontaneous incorporation of gold in palladium-based ternary nanoparticles makes durable electrocatalysts for oxygen reduction reaction. *Nat. Commun.* **7**, 11941 (2016).

14. Klaus, S., Cai, Y., Louie, M. W., Trotochaud, L. & Bell, A. T. Effects of Fe electrolyte impurities on $Ni(OH)_2$/NiOOH structure and oxygen evolution activity. *J. Phys. Chem. C* **119**, 7243-7254 (2015).

15. Lee, S., Bai, L. & Hu, X. Deciphering iron-dependent activity in oxygen evolution catalyzed by nickel iron layered double hydroxide. *Angew. Chem. Int. Ed.* **59**, 8072-8077 (2020).

16. Jiang, J. et al. Atomic-level insight into super-efficient electrocatalytic oxygen evolution on iron and vanadium co-doped nickel (oxy)hydroxide. *Nat. Commun.* **9**, 2885 (2018).

17. Bergmann, A. et al. Unified structural motifs of the catalytically active state of Co(oxyhydr)oxides during the electrochemical oxygen evolution reaction. *Nat. Catal.* **1**, 711-719 (2018).

18. Dionigi, F. et al. In-situ structure and catalytic mechanism of NiFe and CoFe layered double hydroxides during oxygen evolution. *Nat. Commun.* **11**, 2522 (2020).

19. Peña, N. O. et al. Morphological and structural evolution of Co_3O_4 nanoparticles revealed

by in situ electrochemical transmission electron microscopy during electrocatalytic water oxidation. *ACS Nano* **13**, 11372-11381 (2019).

20. Hwang, J. et al. Perovskites in catalysis and electrocatalysis. *Science* **358**, 751–756 (2017).

21. Fabbri, E. et al. Dynamic surface self-reconstruction is the key of highly active perovskite nano-electrocatalysts for water splitting. *Nat. Mater.* **16**, 925-931 (2017).

22. Wu, T. et al. Iron-facilitated dynamic active-site generation on spinel $CoAl_2O_4$ with self-termination of surface reconstruction for water oxidation. *Nat. Catal.* **2**, 763-772 (2019).

23. Zhang, B. et al. Homogeneously dispersed multimetal oxygen-evolving catalysts. *Science* **352**, 333 (2016).

24. Huang, Z.-F. et al. Chemical and structural origin of lattice oxygen oxidation in Co–Zn oxyhydroxide oxygen evolution electrocatalysts. *Nat. Energy* **4**, 329–338 (2019).

25. Kornienko, N. et al. Operando spectroscopic analysis of an amorphous cobalt sulfide hydrogen evolution electrocatalyst. *J. Am. Chem. Soc.* **137**, 7448-7455 (2015).

26. Hu, C. et al. In situ electrochemical production of ultrathin nickel nanosheets for hydrogen evolution electrocatalysis. *Chem* **3**, 122-133 (2017).

27. Zhu, Y. et al. Operando Unraveling of the structural and chemical stability of P-substituted $CoSe_2$ electrocatalysts toward hydrogen and oxygen evolution reactions in alkaline electrolyte. *ACS Energy Lett.* **4**, 987−994 (2019).

28. Zhai, L. et al. In Situ phase transformation on nickel-based selenides for enhanced hydrogen evolution reaction in alkaline medium. *ACS Energy Lett.* **5**, 2483−2491 (2020).

29. Zhang, Y., Gao, L., Hensen, E. J. M. & Hofmann, J. P. Evaluating the stability of Co_2P electrocatalysts in the hydrogen evolution reaction for both acidic and alkaline electrolytes.

ACS Energy Lett. **3**, 1360−1365 (2018).

30. Gamsjäger, H., Bugajski, J., Gajda, T., Lemire, R. J. & Preis, W. *Chemical Thermodynamics of Nickel* (Elsevier Press, 2004).

31. Vaughan, D. J. & Craig, J. R. *Mineral Chemistry of Metal Sulfides* (Cambridge Univ. Press, 1978).

32. Gu, W., Wang, H. & Wang, K. Extended X-ray absorption fine structure and multiple-scattering simulation of nickel dithiolene complexes $Ni[S_2C_2(CF_3)_2]_2^n$ (n = -2, -1, 0) and an olefin adduct $Ni[S_2C_2(CF_3)_2]_2$(1-hexene). *J. Synchrotron Rad.* **22**, 124–129 (2015).

33. Arčon, I., Mirtič, B. & Kodre, A. Determination of valence states of chromium in calcium chromates by using X-ray absorption near-edge structure (XANES) spectroscopy. *J. Am. Ceram. Soc.* **81**, 222-224 (1998).

34. Dau, H., Liebisch, P. & Haumann, M. X-ray absorption spectroscopy to analyze nuclear geometry and electronic structure of biological metal centers-potential and questions examined with special focus on the tetra-nuclear manganese complex of oxygenic photosynthesis. *Anal. Bioanal. Chem.* **376**, 562-583 (2003).

35. Handoko, A. D., Wei, F., Jenndy, Yeo, B. S. & Seh, Z. W. Understanding heterogeneous electrocatalytic carbon dioxide reduction through operando techniques. *Nat. Catal.* **1**, 922-934 (2018).

36. Deng, Y. et al. Operando Raman spectroscopy of amorphous molybdenum sulfide (MoS_x) during the electrochemical hydrogen evolution reaction: Identification of sulphur atoms as catalytically active sites for H^+ reduction. *ACS Catal.* **6**, 7790-7798 (2016).

37. Chen, D.-J. & Tong, Y. Y. J. In situ Raman spectroscopic measurement of near-surface

proton concentration changes during electrochemical reactions. *Chem. Commun.* **51**, 5683-5686 (2015).

38. de las Heras, C. & Agulló-Rueda, F. Raman spectroscopy of $NiSe_2$ and $NiS_{2-x}Se_x$ $(0 < x < 2)$ thin films. *J. Phys. Condens. Matter.* **12**, 5317-5324 (2000).

39. Fateley, W. G., McDevitt, N. T., & Bentley, F. F. Infrared and Raman selection rules for lattice vibrations: The correlation method. *Appl. Spectrosc.* **25**, 155-173 (1971).

40. Cheng, Z., Abernathy, H. & Liu, M. Raman spectroscopy of nickel sulfide Ni_3S_2. *J. Phys. Chem. C* **111**, 17997-18000 (2007).

41. Li, H. et al. Activating and optimizing MoS_2 basal planes for hydrogen evolution through the formation of strained sulphur vacancies. *Nat. Mater.* **15,** 364 (2016).

42. Jiao, Y., Zheng, Y., Davey, K. & Qiao, S.-Z. Activity origin and catalyst design principles for electrocatalytic hydrogen evolution on heteroatom-doped graphene. *Nat. Energy* **1**, 16130 (2016).

43. Voiry, D., Shin, H. S., Loh, K. P. & Chhowalla, M. Low-dimensional catalysts for hydrogen evolution and CO_2 reduction. *Nat. Rev. Chem.* **2**, 0105 (2018).

44. Vrubel. H., Moehl, T., Grätzel, M. & Hu, X. Revealing and accelerating slow electron transport in amorphous molybdenum sulphide particles for hydrogen evolution reaction. *Chem. Commun.* **49**, 8985-8987 (2013).

45. Wei, C. et al. Recommended practices and benchmark activity for hydrogen and oxygen electrocatalysis in water splitting and fuel cells. *Adv. Mater.* **31**, 1806296 (2019).

46. Deml, A. M., Stevanović, V., Muhich, C. L., Musgrave, C. B. & O'Hayre, R. Oxide enthalpy of formation and band gap energy as accurate descriptors of oxygen vacancy formation energetics. *Energy Environ. Sci.* **7**, 1996-2004 (2014).

47. Newville, M. IFEFFIT: interactive XAFS analysis and FEFF fitting. *J. Synchrotron Radiat.* **8**, 322–324 (2001).

48. Kresse, G. & Hafner, J. Ab initio molecular-dynamics simulation of the liquid-metal-amorphous-semiconductor transition in germanium. *Phys. Rev. B* **49**, 14251-14269 (1994).

49. Perdew, J. P., Burke, K. & Ernzerhof, M. Generalized gradient approximation made simple. *Phys. Rev. Lett.* **77**, 3865-3868 (1996).

Author contributions

Z.K. and Y.Z. designed and proposed the research direction, initiated and supervised the project. Y.S. performed the experiments. J.W. carried out the DFT simulations. Y.S. and Z.Z. designed and analysed the in-situ Raman and XAFS measurements. X.W., B.L. and Y.X. assisted with XAFS experiments and discussions about DFT simulations. J.W. and Z.K. contributed to the analysis of electrochemical performance. Q.L., S.Z., Y.Q.Z. and K.M. assisted in carrying out the XRD, SEM, XPS, TEM and EDS measurements. All the authors discussed the results and participated in writing the manuscript.

Competing interests

The authors declare no competing interests.

1 **Supplementary Information**

2

3 **Phase reconfiguration of multivalent nickel sulfides in hydrogen evolution**

4

5 Yu Sun[1,2,3], Jing Wu[1,2,3], Zheng Zhang[1,2,3], Qingliang Liao[1,2], Suicai Zhang[1,2], Xin Wang[1,2],

6 Baishan Liu[1,2], Yunqi Zhao[1,2], Yong Xie[1,2], Kaikai Ma[1,2], Zhuo Kang[*][1,2] and Yue Zhang[*][1,2]

7

8 [1]Beijing Advanced Innovation Center for Materials Genome Engineering, Beijing Key

9 Laboratory for Advanced Energy Materials and Technologies, University of Science and

10 Technology Beijing, Beijing 100083, China

11 [2]State Key Laboratory for Advanced Metals and Materials, School of Materials Science and

12 Engineering, University of Science and Technology Beijing, Beijing 100083, China

13 [3]These authors contributed equally: Yu Sun, Jing Wu, Zheng Zhang.

14 *e-mail: zhuokang@ustb.edu.cn; yuezhang@ustb.edu.cn

15

16

17

18

19

20

21 **Table of Contents:**

24

25

26

27

28

Supplementary Figures
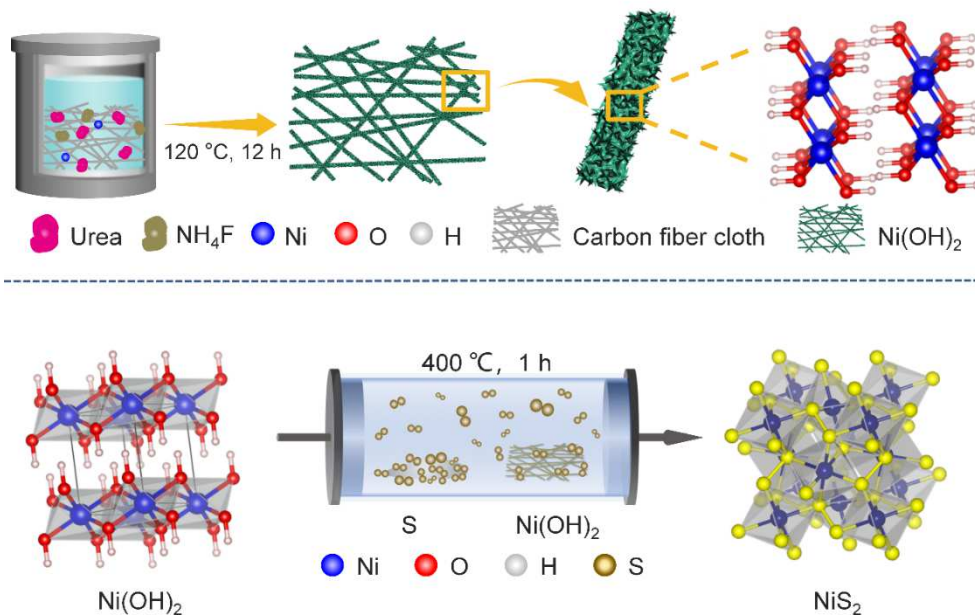
Supplementary Fig. 1. Fabrication of $Ni_{1-x}Fe_xS_2$/CFP H_2-evolving electrodes. Schematic illustration of the fabrication procedure by directly growing $Ni_{1-x}Fe_xS_2$ NSs, and the sulfurization process at 400 °C.
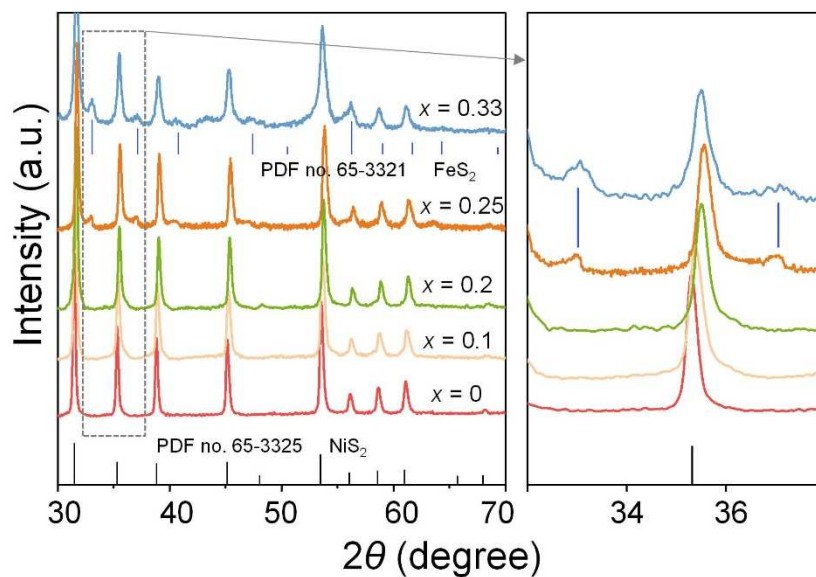

Supplementary Fig. 2. PXRD patterns of synthesized $Ni_{1-x}Fe_xS_2$ ($x \approx$ 0-0.33). The right axis show the unit cell of cubic metal disulfides and the magnified PXRD patterns in the range between 32 and 38.
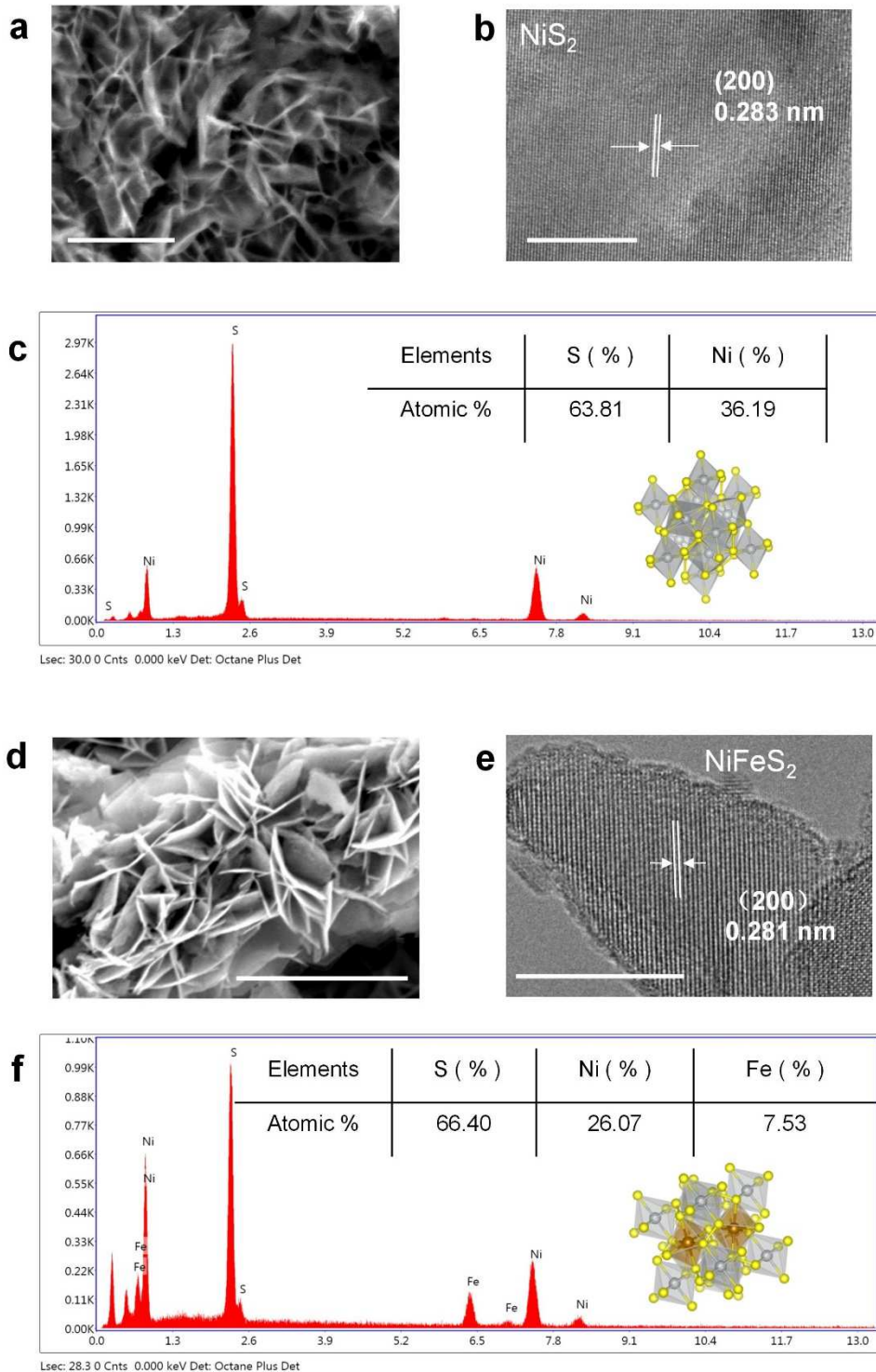
Supplementary Fig. 3. SEM-EDX elemental analysis and the TEM images of the as-prepared $Ni_{1-x}Fe_xS_2$ electrode. a, SEM images of the carbon fiber coated with NiS_2. Scale bar, 1 μm. b, TEM images of NiS_2 NSs. Scale bar, 5 nm. c, The corresponding EDX elemental atomic ratio of Ni and S elements. d, Top-view SEM images of the carbon fiber coated with $Ni_{0.8}Fe_{0.2}S_2$ NSs. Scale bar, 10 μm. e, TEM images of $Ni_{0.8}Fe_{0.2}S_2$ NSs. Scale bar, 10 nm. f, The corresponding EDX elemental atomic ratio of Ni, Fe and S elements. Inset of c and f is the corresponding weight and atomic ratio of Ni, Fe and S elements and the lattice structure of $Ni_{1-x}Fe_xS_2$.
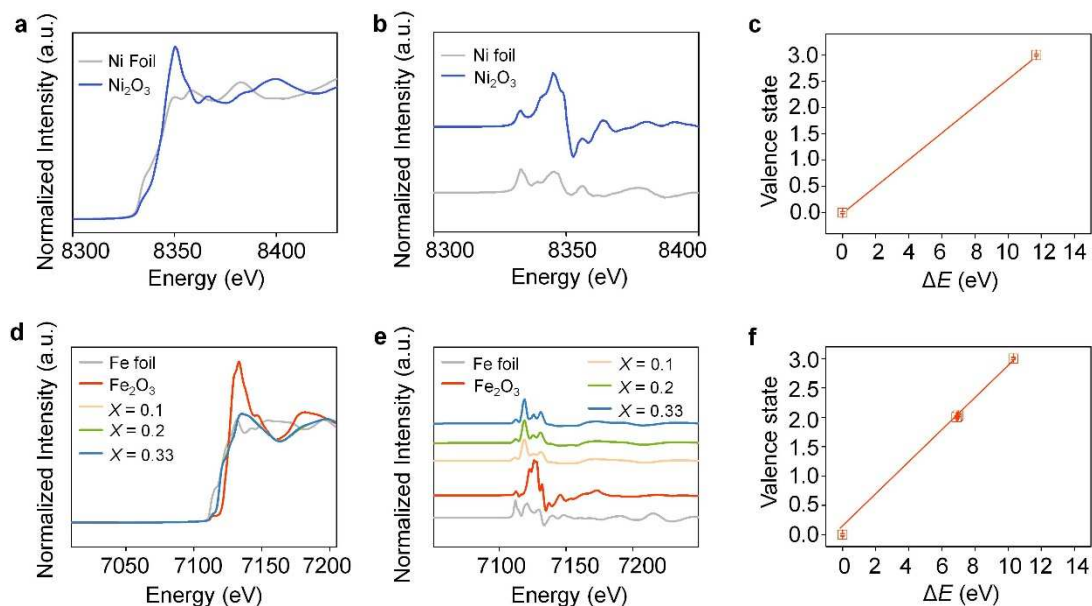
Supplementary Fig. 4. XAFS measurements. a, XANES spectra recorded at the Ni K-edge of nickel foil, Ni_2O_3. b, Normalized difference spectra for Ni K-edge XANES. c, The fitted average valence states of Ni from XANES spectra. Ni Foil is approximately close to 0, Ni_2O_3 is approximately close to 3+. d, XANES spectra recorded at the Fe K-edge of Iron foil, Fe_2O_3. e, Normalized difference spectra for Fe K-edge XANES. f, The fitted average valence states of Fe from XANES spectra. Fe Foil is approximately close to 0, Fe_2O_3 is approximately close to 3+. Error bars represent the standard deviation from at least three independent measurements.

The Ni and Fe valence states of the samples were estimated by means of the absorption edge energy E_0, which is defined as the energy at the highest first derivative of the absorbance as shown in Supplementary Fig. 4b, e. Correspondingly, the absorption edge energy E_0 of Ni foil with Ni^0 valence state is determined as 8333 eV as shown in Supplementary Fig. 4b. Similarly, the Ni K-edge EXAFS spectra show that the absorption edge energies E_0 of the NiS_2, $Ni_{0.9}Fe_{0.1}S_2$, $Ni_{0.8}Fe_{0.2}S_2$, and $Ni_{0.67}Fe_{0.33}S_2$ and Ni_2O_3 were located at 8360.68, 8340.35, 8340.12, and 8340.27 and 8344.61 eV, respectively. The Fe K-edge EXAFS spectra show that the absorption edge energies E_0 of the Fe Foil, $Ni_{0.9}Fe_{0.1}S_2$, $Ni_{0.8}Fe_{0.2}S_2$, and $Ni_{0.67}Fe_{0.33}S_2$ and Fe_2O_3 were located at 7112, 7118.92, 7118.98, 7118.89 and 7122.32 eV, respectively.

The obtained energy shifts (ΔE), as a function of the valence state, are shown in Supplement Fig. 4c, f, together with a model linear function, which have been determined as a best fit to the data from the reference samples. The nickel and iron valence states in the synthesized Fe substituted nickel sulfides are calculated from the linear function. These data are listed in Supplementary Table 1.

1
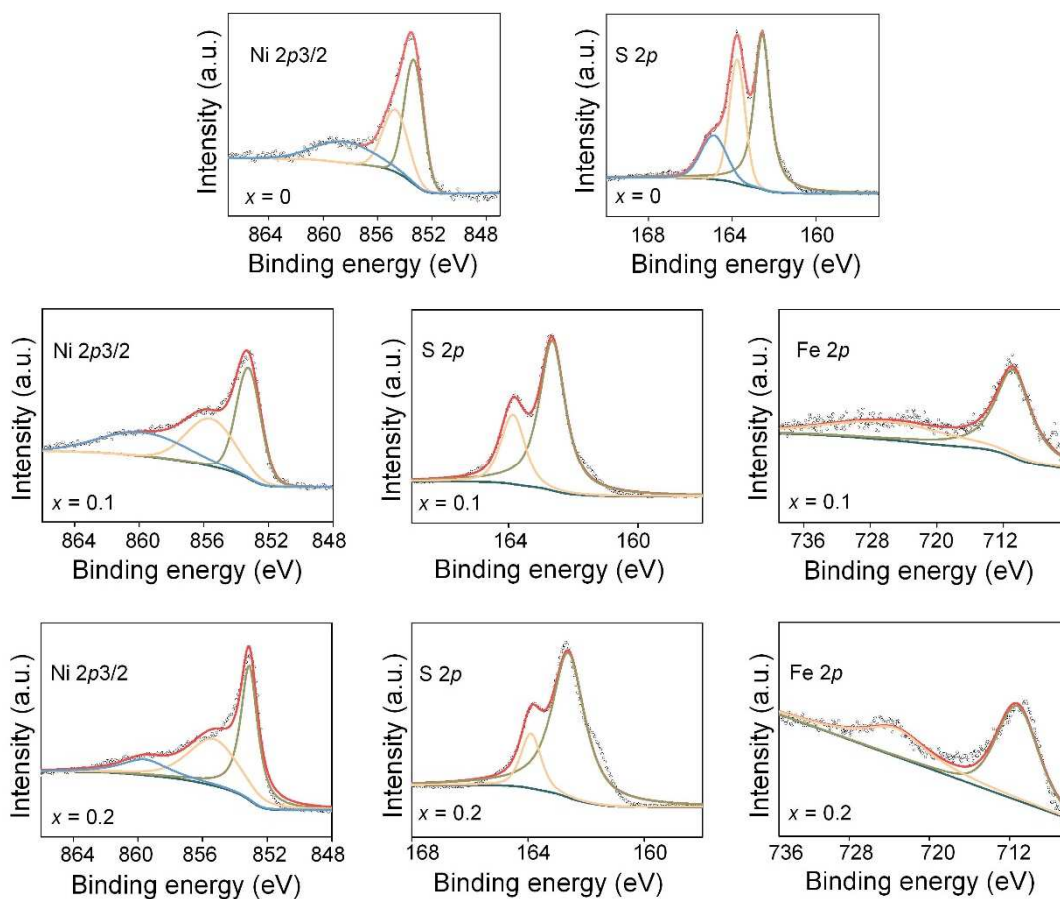
Supplementary Fig. 5. XPS Characterization of $Ni_{1-x}Fe_xS_2$ ($x = 0, 0.1, 0.2$) for the Ni $2p3/2$, S $2p$ and Fe $2p$ regions. The broad S $2p$ XPS peak is fitted into two main peaks. The peaks located at 162.6 and 163.8 eV are attributed to the S $2p3/2$ and S $2p1/2$ orbitals of bridging S_2^{2-}.

5

6

7

8

9

10

11

12

13

14

1
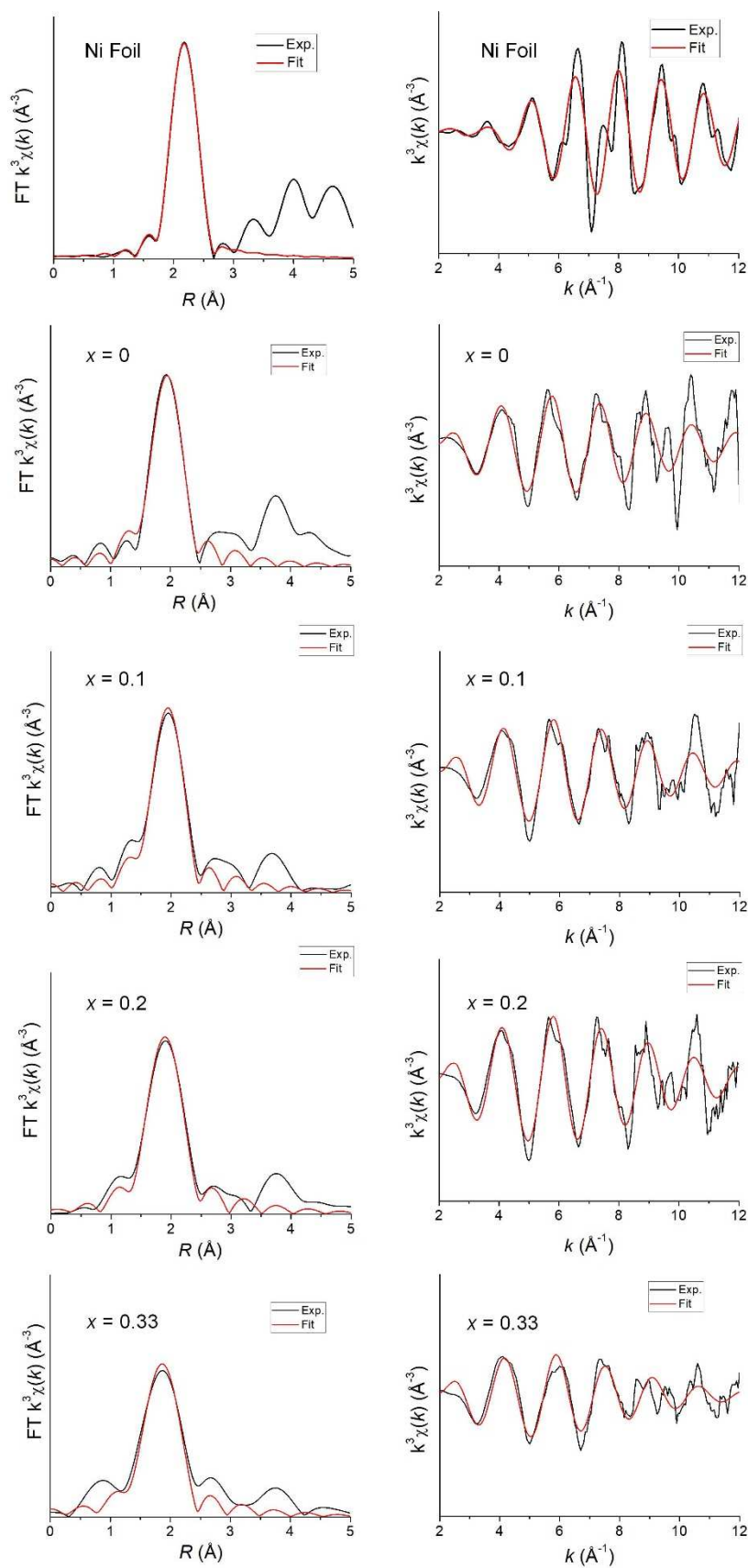
Supplementary Fig. 6. Ni K-edge EXAFS analysis of samples in R and k spaces. FT-EXAFS spectra and
fits of Ni K-edges from Ni foil and $Ni_{1-x}Fe_xS_2$ ($x = 0, 0.1, 0.2, 0.33$) catalysts. The black lines represent the
experiment data and the red lines represent the fitting values.
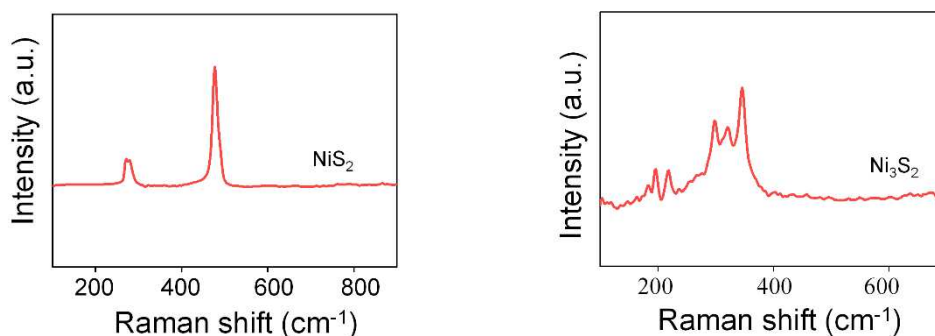
Supplementary Fig. 7. Raman spectrum of NiS_2 and Ni_3S_2. The peaks at 274.4(T_g), 284.8(E_g), 479.3(A_g) cm^{-1} previously attributed to NiS_2, peaks at 187.6 ($A_1(2)$), 202.1 ($E(4)$), 223.6 ($E(3)$), 303.6 ($E(2)$), 324.6 ($A_1(1)$), 350.3 ($E(1)$) cm^{-1} were correlated respectively with two A_1 stretching and four E bending vibration of Ni-S in the heazlewoodite-phase Ni_3S_2, the peaks are shown in Supplementary Table 4.
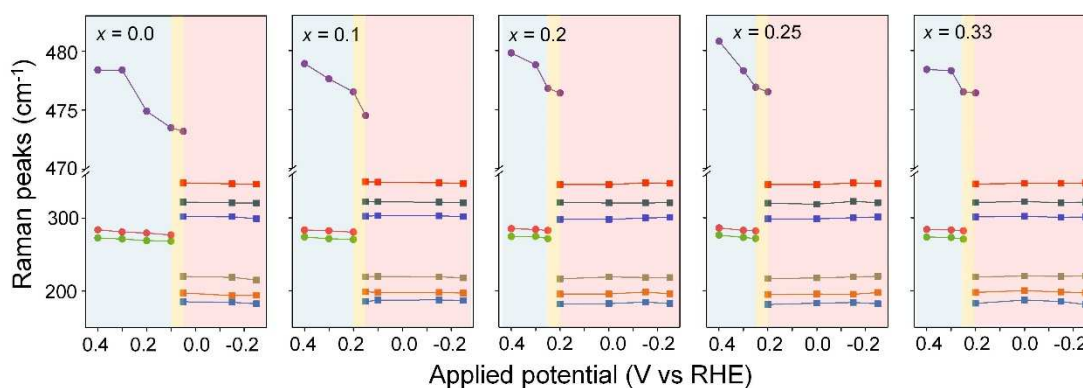

Supplementary Fig. 8. Frequency of the vibrational modes versus the applied potential obtained from the in-situ Raman spectra for $Ni_{1-x}Fe_xS_2$.
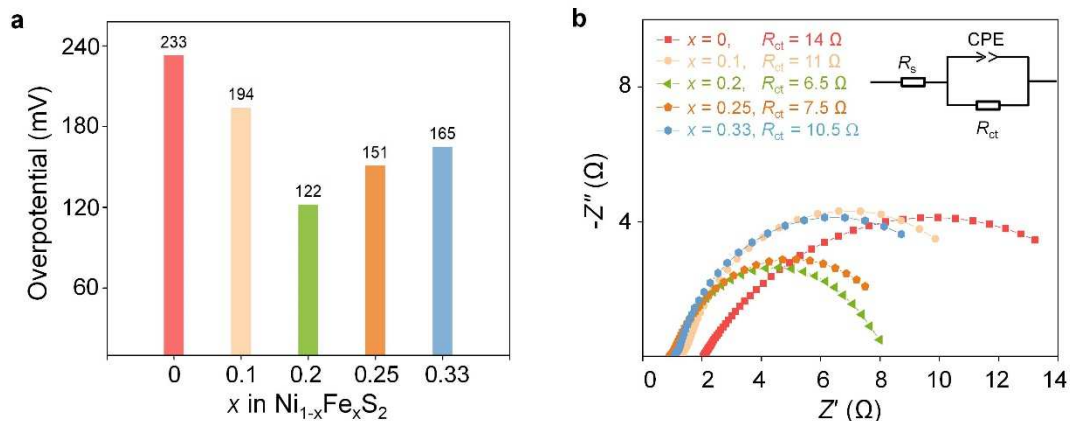
Supplementary Fig. 9. Electrochemical characterization of $Ni_{1-x}Fe_xS_2$. a, Overpotential of the nickel sulfide catalysts at the current density of 10 mAcm^{-2}, b, Nyquist plots of the catalyst electrode @200 mV overpotential in 1M KOH. Inset of (b) is the simplified Randles equivalent circuit model. The intercept in the high frequency zone are attributed to the internal charge-transfer resistances or the system resistance (R_s) of electrodes, and the semicircles represent the charge transfer resistances (R_{ct}) at the electrode/electrolyte interface. The charge-transfer resistances (R_{ct}) measured at 200 mV overpotential are 14, 11, 6.5, 7.5 and 10.5 Ω for the CFP-supported pure NiS_2, $Ni_{0.9}Fe_{0.1}S_2$, $Ni_{0.8}Fe_{0.2}S_2$, $Ni_{0.75}Fe_{0.25}S_2$ and $Ni_{0.67}Fe_{0.33}S_2$, respectively.
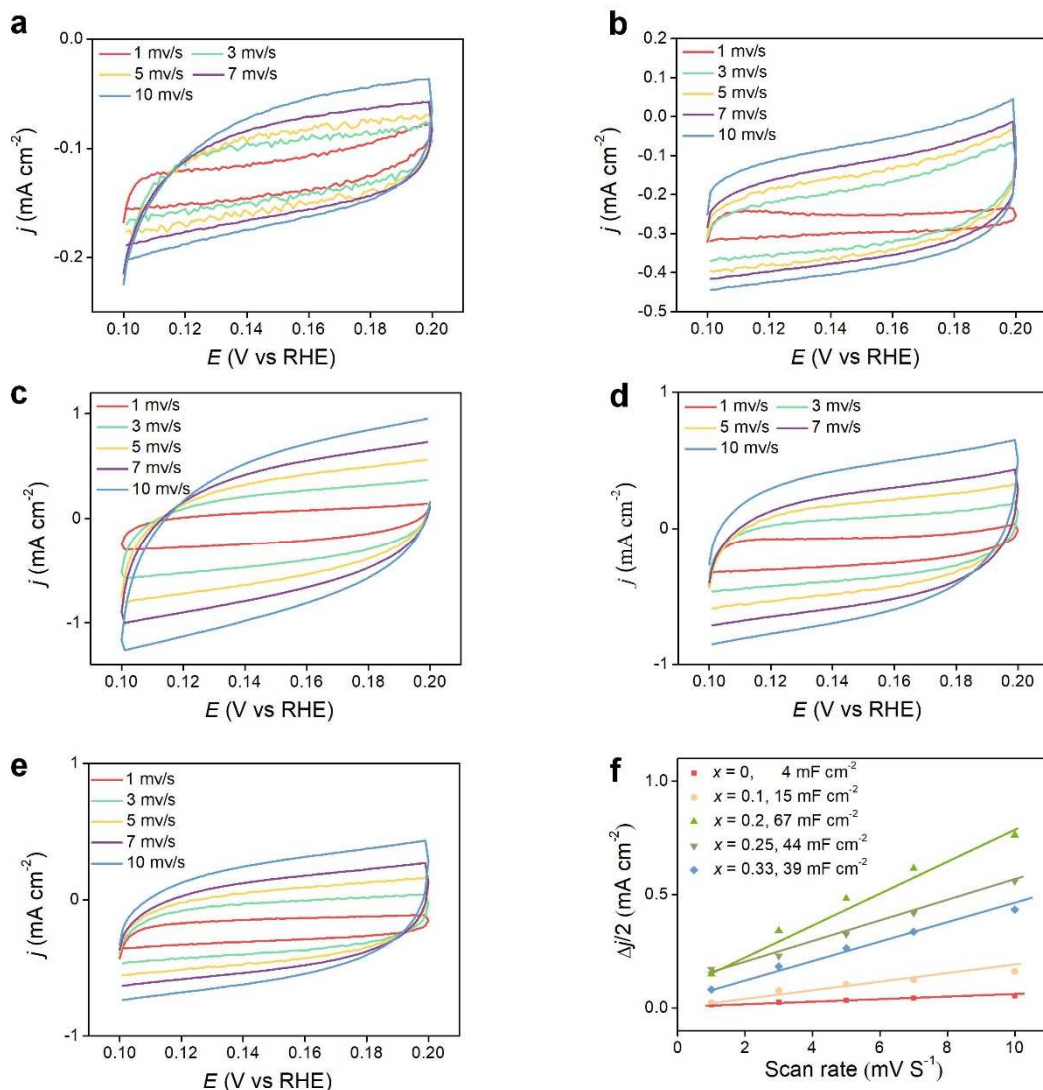
Supplementary Fig. 10. Cyclic voltammograms of the as-fabricated nickel sulfide catalysts. Cyclic voltammograms at different scan rates of in the non-Faradaic potential region (0.1 to 0.2 V versus RHE) for the $Ni_{1-x}Fe_xS_2$ (a, $x = 0$; b, $x = 0.1$; c, $x = 0.2$; d, $x = 0.25$; e, $x = 0.33$) catalysts in 1 M KOH at different scan rates (1, 3, 5, 7, 10 mV s^{-1}). f, Charging current density differences at 0.15 V versus RHE plotted against scan rate. The value of C_{dl} was estimated from the slope of the linear relationship between the half capacitive current density ((j_{anodic} -$j_{cathodic}$)/2) at the middle of the applied potential range and the scan rates. Significantly, the $Ni_{0.8}Fe_{0.2}S_2$ yields an extremely high C_{dl} value up to 67 mF cm^{-2}, considerably larger than those of the NiS_2 (4 mF cm^{-2}), $Ni_{0.9}Fe_{0.1}S_2$ (15 mF cm^{-2}), $Ni_{0.75}Fe_{0.25}S_2$ (44 mF cm^{-2}) and $Ni_{0.67}Fe_{0.33}S_2$ (39 mF cm^{-2}), which indicates that an appropriate concentration of Fe doping can substantially extend the electrochemical active area and render more catalytic active sites.
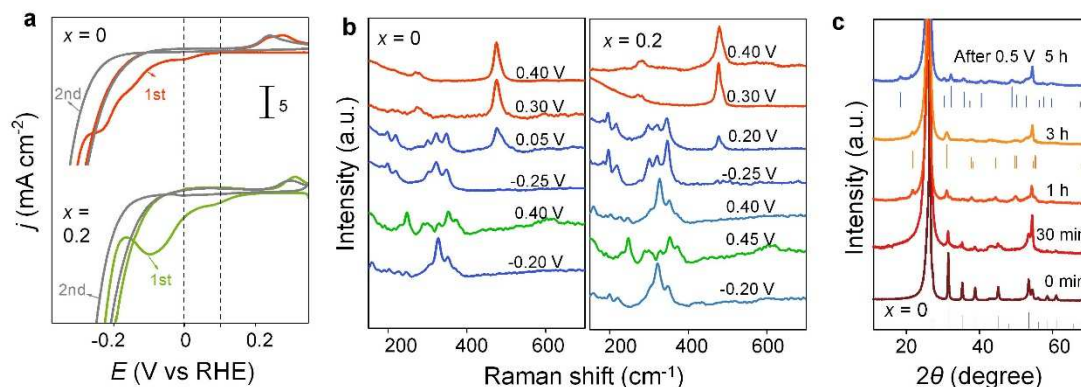
Supplementary Fig. 11. a, Cyclic Voltammetry curves of $Ni_{1-x}Fe_xS_2$ (x = 0.0, 0.2) in N_2-saturated 1 M KOH with a scan rate of 2 mV s^{-1} between 0.4 and -0.4 V (vs. RHE) to show the pseudocapacitive behavior preceding to HER. b, In-situ Raman spectra of $Ni_{1-x}Fe_xS_2$ (x = 0 and 0.2) at the potentials of 0.45 V~-0.25 V (RHE) in 1M KOH. c, XRD patterns of catalyst after the operation of HER instantly at constant current density of -10 mA cm^{-2} and constant potential 0.5 V (RHE) 5 h. We can interpret that NiS_2 have a phase transition to Ni_3S_2 under the proper conditions, and it will have a reversible phase transition to β-NiS.

For the CV curves of oxidation scan, nickel sulfides all have an anodic peak. In-situ Raman spectra and XRD patterns prove the structure will have a phase transition to β-NiS structure with the potential increase. The anodic peak of $Ni_{0.8}Fe_{0.2}S_2$ is higher than that of NiS_2 in the CVs, which means the more stability in the Fe substitution.
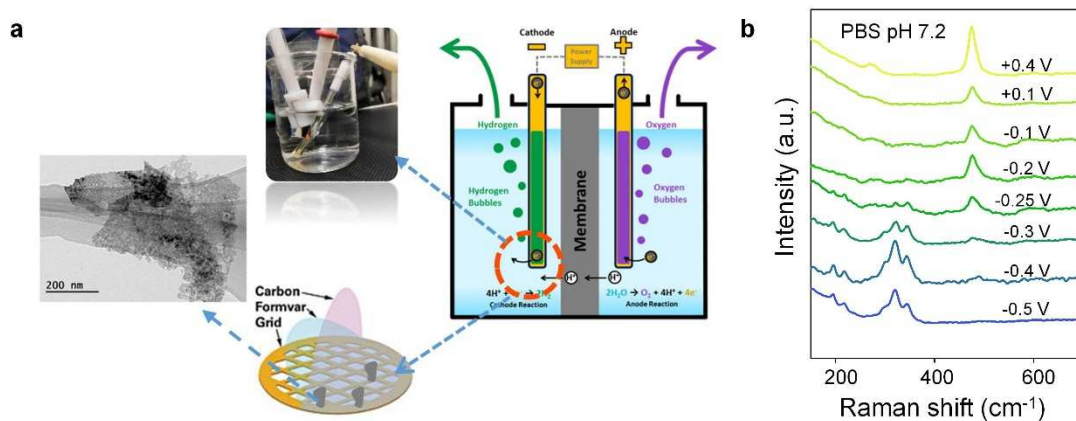
Supplementary Fig. 12. TEM characterization of surface-restructured nickel sulfide after the process of HER. a, Schematic process of HRTEM of nickel sulfide. b, In-situ Raman spectra of NiS_2 at the potentials of 0.4 V~-0.5 V (RHE) in 0.01M PBS (NaPi, pH7.2).

The catalysts sprayed on the Cu grids, which were attached to the Au electrode with conductive carbon tape, polarized in N_2 saturated 0.01 M NaPi electrolyte (pH 7.2) at the potential of -0.45 V (vs RHE) for 2 h. As we can see the results from different condition of electrolyte, reconstruction potential range turned on, which is -0.25~-0.3V for 0.01M NaPi.
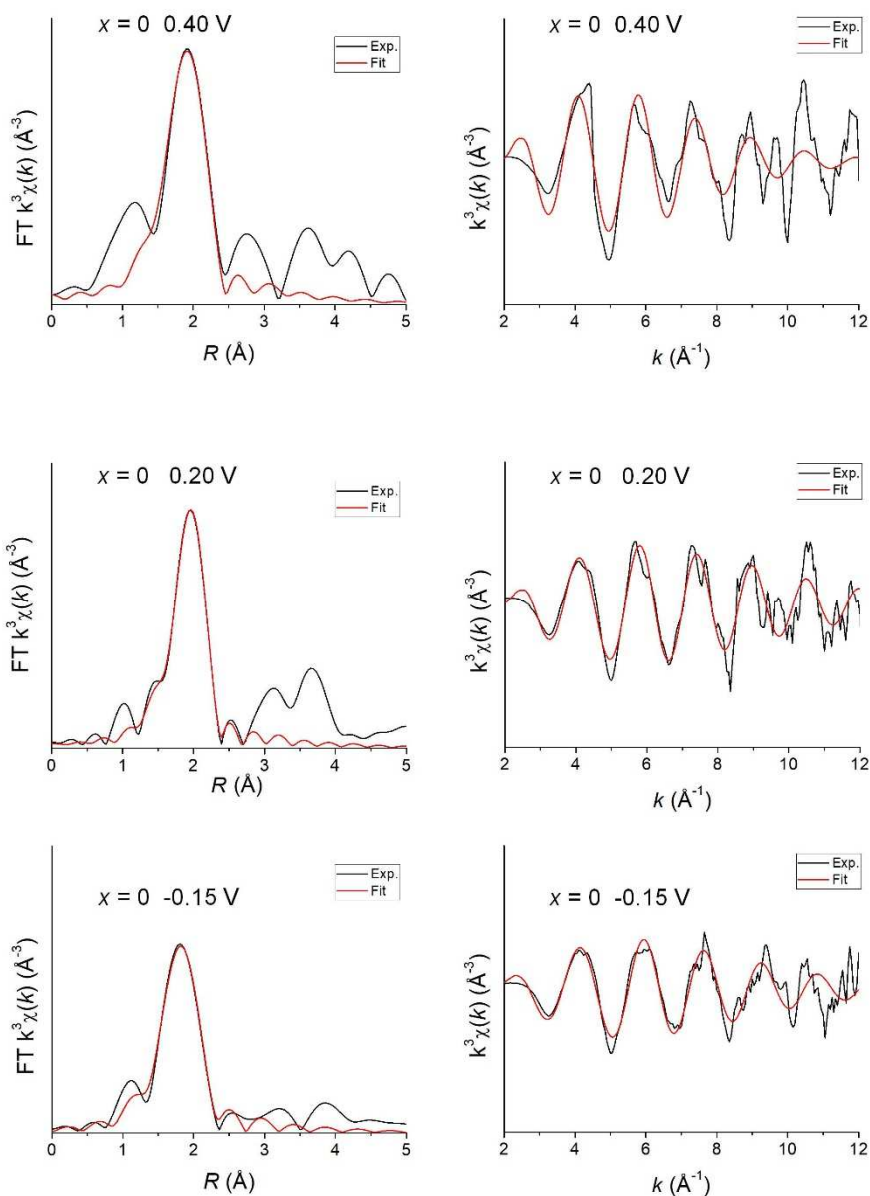
1

2

3 **Supplementary Fig.13.** Ni K-edge EXAFS analysis of nickel sulfide in *R* and *k* spaces. FT-EXAFS spectra

4 and fits of Ni K-edges from NiS$_2$ (in -0.15V, 0.20 V and 0.40 V vs RHE test). The black lines represent the

5 experiment data and the red lines represent the fitting values.

1
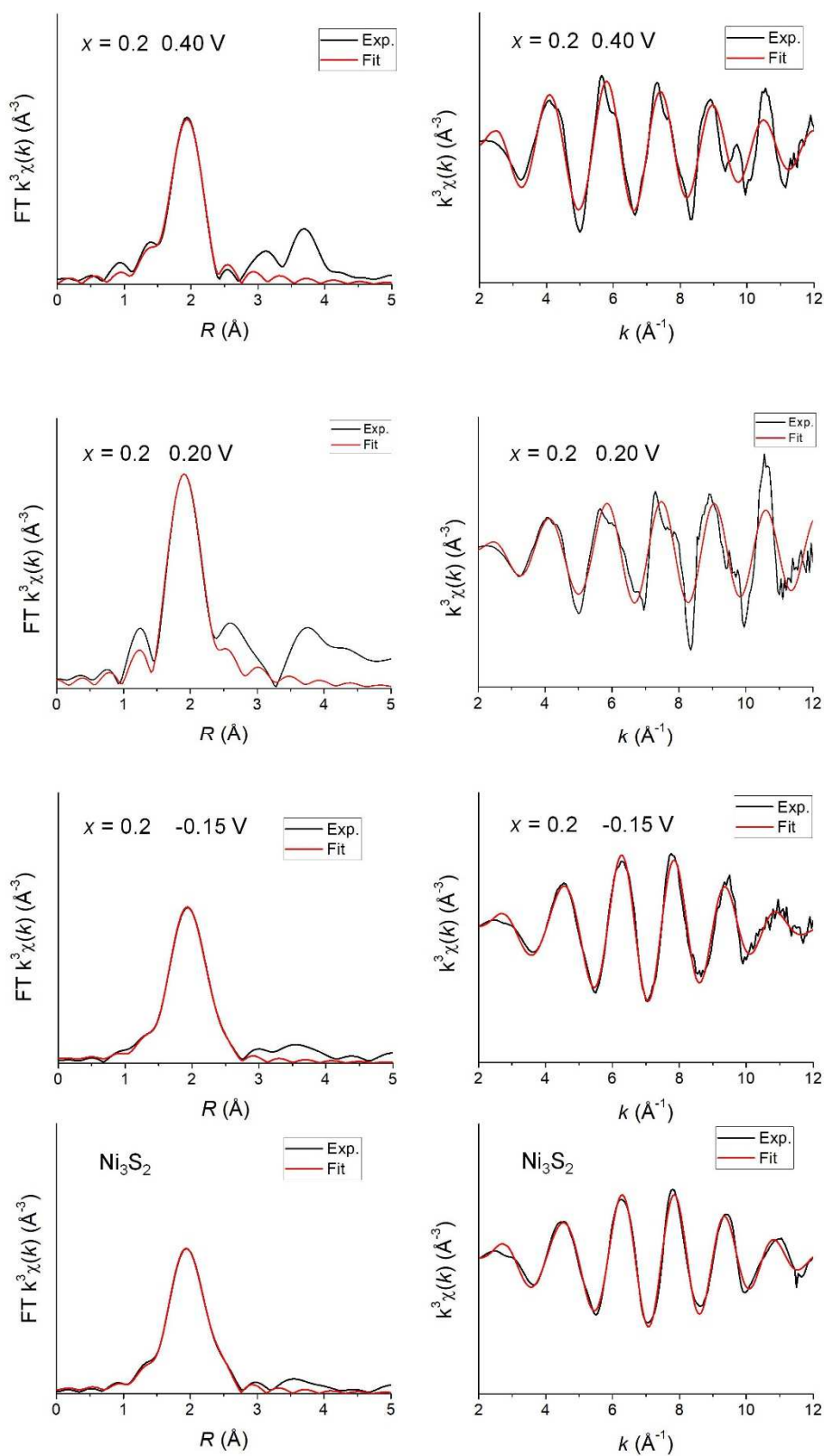
2 **Supplementary Fig. 14.** Ni K-edge EXAFS analysis of nickel sulfide in R and k spaces. FT-EXAFS spectra

3 and fits of Ni K-edges from Ni_3S_2 catalysts and $Ni_{0.8}Fe_{0.2}S_2$ (in -0.15 V, 0.20 V and 0.40 V vs RHE test). The
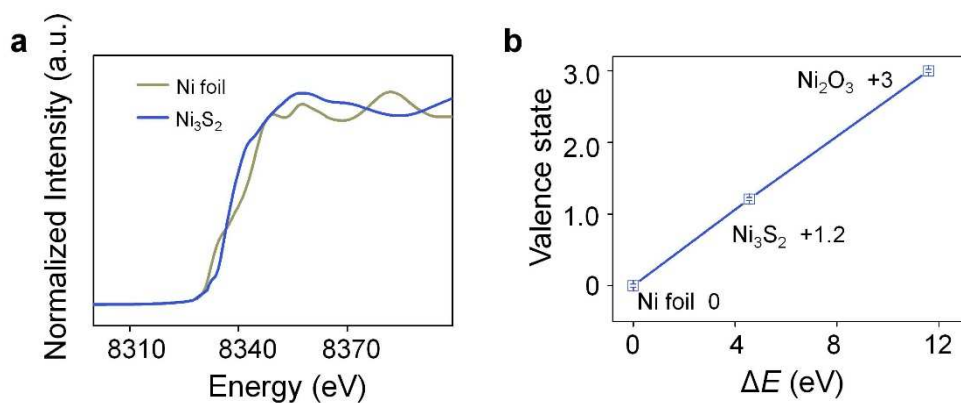
4 black lines represent the experiment data and the red lines represent the fitting values.

5

a

Normalized Intensity (a.u.)

— Ni foil
— Ni_3S_2

8310   8340   8370
Energy (eV)

b

Valence state

3.0 Ni_2O_3 +3
2.0
1.0 Ni_3S_2 +1.2
0   Ni foil 0

0   4   8   12
ΔE (eV)

1

2 **Supplementary Fig. 15.** XAFS measurements. a, b is the Ni_3S_2 XANES spectra and the corresponding
3 valence state of Ni in Ni_3S_2 according to the linear relationship described in b. Error bars represent the
4 standard deviation from at least three independent measurements. The average valence state of nickel foil
5 and Ni_2O_3 is fitted to 0 and +3 by the Nickel K-edge XANES in Supplementary Fig. 4. Applying the linear
6 correlation, it is found that the average valence state of Ni for Ni_3S_2 is approximately +1.20.

7

8

9

10

11

12

13

14

15

1
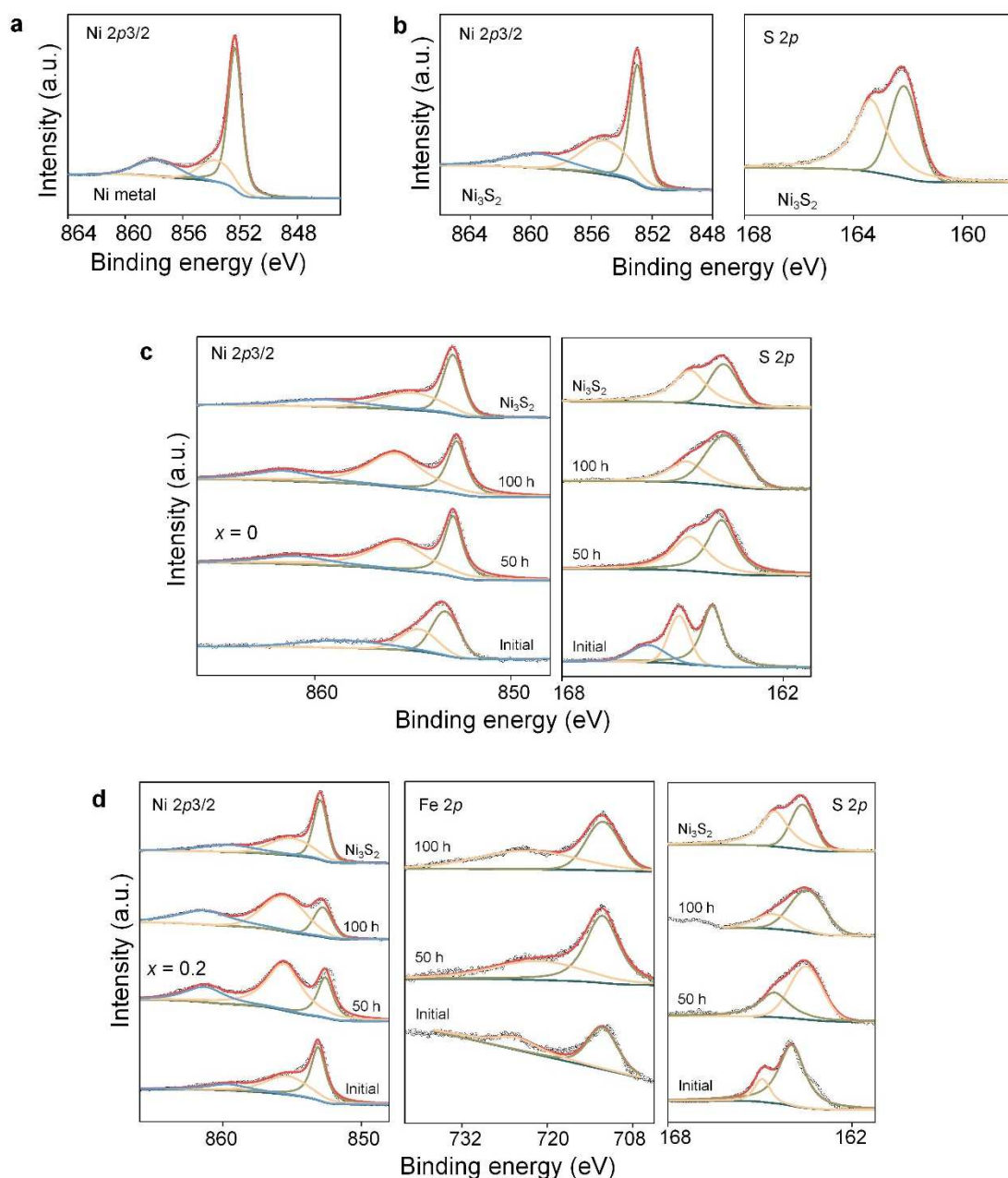
Supplementary Fig. 16. XPS Characterization. a, Ni Metal of Ni $2p3/2$ regions. b, Ni $2p3/2$ and S $2p$ regions of Ni_3S_2. The Ni metal peak at 852.30 eV, and the Ni peak of Ni_3S_2 is about at 852.85 eV. c, d, XPS analysis of the electrodes after long time test as the work electrode to identify the binding energy and ratio of the surface element for NiS_2 (c) and $Ni_{0.8}Fe_{0.2}S_2$ (d). At 50 h and 100 h, the Ni $2p3/2$ binding energy is approaching to Ni in Ni_3S_2, while for Fe, the binding energy is slightly changed.

For the Ni $2p2/3$, the peaks after 50 h and 100 h are all verge on the corresponding peaks of the Ni_3S_2 crystal, thus implying the finalized phase of the long-term service also close to Ni_3S_2 structure.
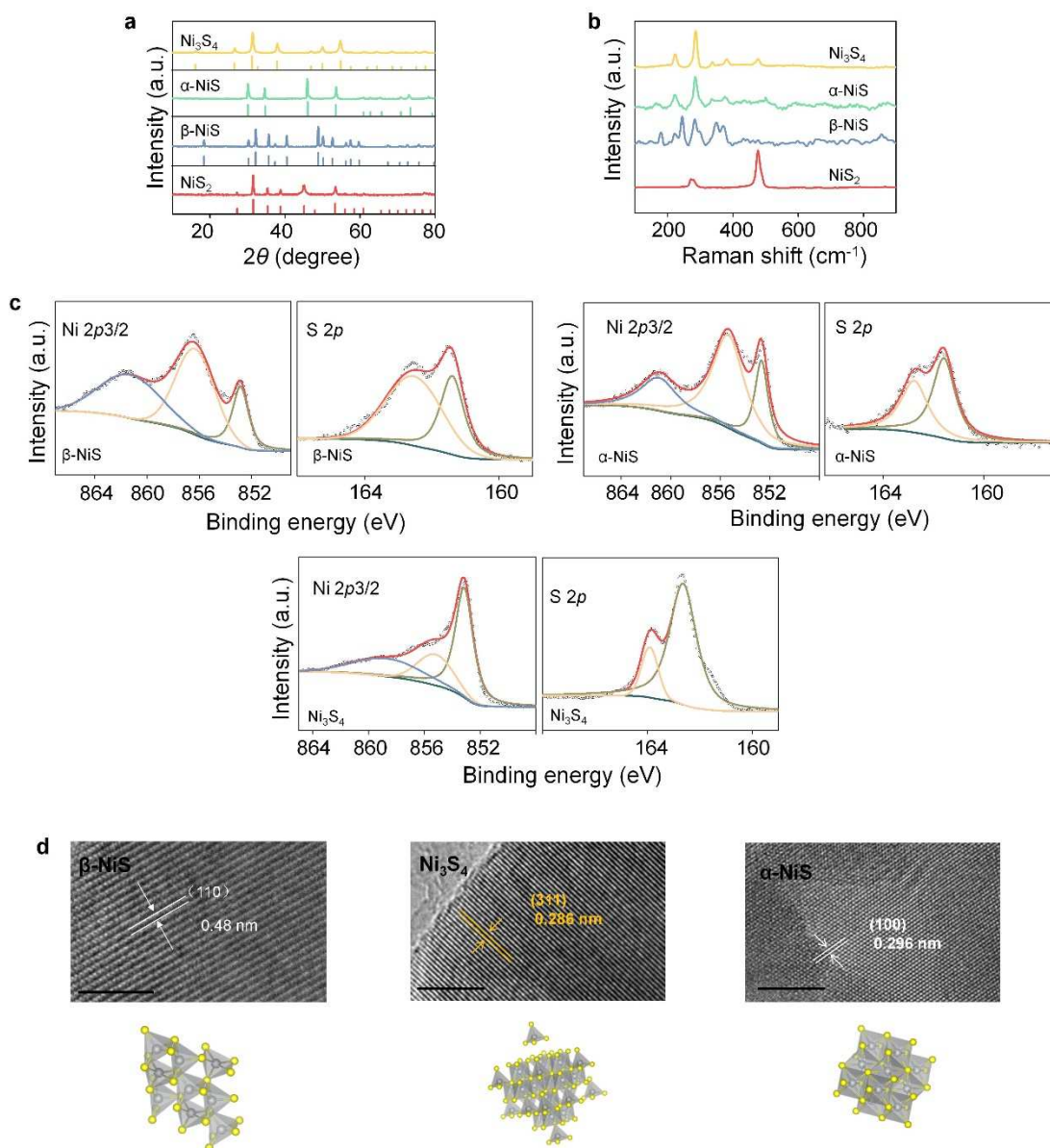
Supplementary Fig. 17. Structure Characterization of α-NiS, β-NiS Ni$_3$S$_4$. a PXRD, b Raman spectra. The PDF number of β-NiS is 12-0041, the PDF number of α-NiS is 02-1280, the PDF number of Ni$_3$S$_4$ is 43-1469; the Raman peaks are shown in Table 4. c, XPS analysis of the electrodes of α-NiS, β-NiS and Ni$_3$S$_4$. d, HRTEM characterization of α-NiS, β-NiS and Ni$_3$S$_4$ and the lattice structure of each Nickel sulfides. Scale bars, 5 nm. For spinel structure of Ni$_3$S$_4$, there is two arrangement of Ni atom and S atom to consist octahedron polyhedral of Ni with six S around and tetrahedron polyhedral of Ni with four S. For β-NiS, there is five S around Ni atom to consist pyramidal polyhedral. For the α-NiS, the Ni atom is around with six S atom to consist octahedron polyhedral.
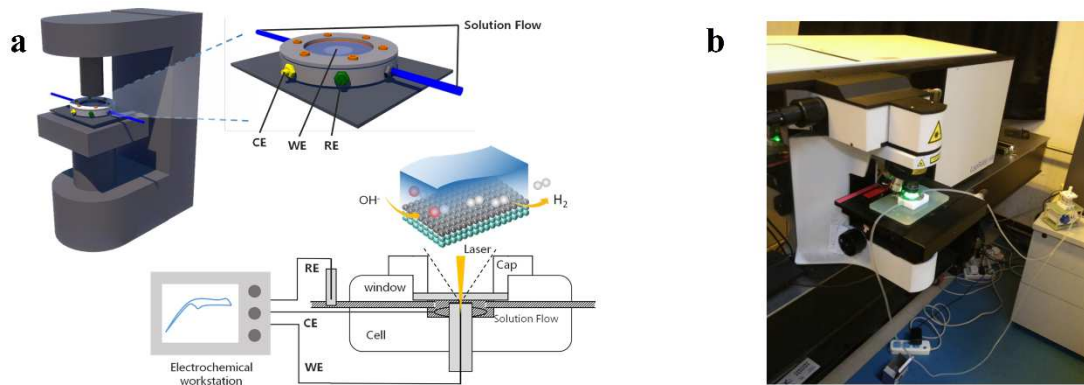
Supplementary Fig. 18. Equipment used for in-situ Raman measurements. a, Schematic for the equipment used for in-situ Raman. b, Digital photo taken during in-situ Raman.
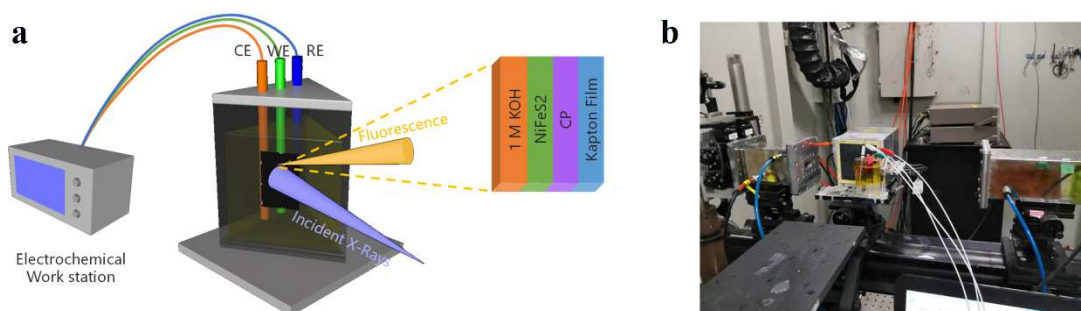
Supplementary Fig. 19. Equipment used for operando XAFS measurements. a, Schematic for the equipment used for operando XAFS measurements. b, Digital photo taken during operando XAFS measurement.

Supplementary Tables

Supplementary Table 1. The Ni and Fe K-edge positions, nominal Ni and Fe valence state and the nominal sulphur vacancy concentration (δ) in $Ni_{1-x}Fe_xS_{2-\delta}$.

Samples	Fe k-edge		Samples	Ni k-edge		Nominal sulphur vacancy concentration (δ)
	Edge energy (eV)	Nominal Valence state		Edge energy (eV)	Nominal Valence state	
Fe foil	7112.00	0.00	Ni foil	8333.00	0.00	
Fe_2O_3	7122.32	3.00	Ni_2O_3	8344.61	3.00	
			$x = 0$	8340.68	1.98	$\delta = 0.02$ ($NiS_{1.98}$)
$x = 0.1$	7118.92	2.01	$x = 0.1$	8340.35	1.90	$\delta = 0.09$ ($Ni_{0.9}Fe_{0.1}S_{1.91}$)
$x = 0.2$	7118.98	2.03	$x = 0.2$	8340.12	1.84	$\delta = 0.13$ ($Ni_{0.8}Fe_{0.2}S_{1.87}$)
$x = 0.33$	7118.89	2.00	$x = 0.33$	8340.27	1.88	$\delta = 0.08$ ($Ni_{0.67}Fe_{0.33}S_{1.92}$)

The nominal sulphur vacancy concentration was calculated on the basis of the nominal valence state of Ni, Fe and S.

Supplementary Table 2. XPS fitting parameters of binding energies for the as-prepared nickel sulfide catalysts.

Catalyst	Binding energy (eV)					Element Ratio (%) Ni : (Fe): S
	Ni 2p3/2	S 2p3/2	S 2p1/2	Fe 2p3/2	Fe 2p1/2	
Ni Metal	852.30	—	—	—	—	—
Ni_3S_2	852.82	162.18	163.36	—	—	23.85:27.57
NiS_2	853.56	162.58	163.79	—	—	4.01:10.26
$Ni_{0.9}Fe_{0.1}S_2$	853.13	162.7	163.8	710.87	726.92	8.69: (1.03): 20.24
$Ni_{0.8}Fe_{0.2}S_2$	853.16	162.63	163.92	710.65	722.85	10.52: (1.47) : 21.05
NiS_2, 50 h	852.89	162.26	163.43	—	—	26.03:16.33
NiS_2, 100 h	852.68	162.25	163.80	—	—	22.92:13.28
$Ni_{0.8}Fe_{0.2}S_2$, 50 h	852.59/ 855.56	162.25	163.48	711.05	722.08	20.09: (1.16): 10.27
$Ni_{0.8}Fe_{0.2}S_2$, 100 h	852.77/ 855.50	162.10	163.47	711.12	722.28	21.02: (0.95) : 16.20
α-NiS	852.71/ 855.38	161.59	162.79	—	—	16.42:10.84
β-NiS	852.89/ 856.52	161.41	162.60	—	—	10.36:14.93
Ni_3S_4	853.17/ 855.32	162.68	163.90	—	—	13.32:35.22

3

4

5

6

7

8

9

10

11

12

Supplementary Table 3. EXAFS fitting parameters at the Ni K-edge various samples（S_0^2 = 0.82）

Sample	Path	CN[a]	R (Å)[b]	$\sigma^2 \times 10^{-3}$ (Å²)[c]	ΔE (eV)[d]	R factor
Ni foil	Ni-Ni	12*	2.48 ± 0.01	6.1 ± 0.2	6.7 ± 0.3	0.001
x = 0	Ni-S	6.0 ± 0.7	2.40 ± 0.01	7.4 ± 1.8	2.0 ± 1.9	0.015
x = 0.1	Ni-S	5.9 ± 0.6	2.39 ± 0.01	8.2 ± 1.5	3.5 ± 1.5	0.010
x = 0.2	Ni-S	5.8 ± 0.6	2.38 ± 0.01	8.2 ± 2.1	1.4 ± 1.8	0.007
x = 0.33	Ni-S	5.4 ± 0.6	2.36 ± 0.02	10.9 ± 3.2	1.6 ± 2.7	0.016
Ni₃S₂	Ni-S	3.9 ± 0.4	2.27 ± 0.02	6.8 ± 2.4	3.8 ± 1.6	0.001
	Ni-Ni	2.0 ± 1.1	2.52 ± 0.03	6.2 ± 4.0	4.6 ± 4.6	
x = 0.2 0.40 V	Ni-S	5.9 ± 0.6	2.38 ± 0.01	7.3 ± 0.9	1.3 ± 1.1	0.008
x = 0.2 0.20 V	Ni-S	4.1 ± 0.4	2.36 ± 0.01	2.5 ± 1.6	0.9 ± 2.2	0.011
x = 0.2 -0.15 V	Ni-S	3.5 ± 0.4	2.26 ± 0.02	6.2 ± 2.5	2.4 ± 2.2	0.001
	Ni-Ni	2.8 ± 1.6	2.51 ± 0.03	7.7 ± 4.5	0.1 ± 5.9	
x = 0 0.40 V	Ni-S	6.0 ± 0.7	2.39 ± 0.01	4.6 ± 1.3	1.5 ± 1.8	0.018
x = 0 0.20 V	Ni-S	6.0 ± 0.6	2.38 ± 0.01	6.1 ± 1.4	1.4 ± 1.1	0.016
x = 0 -0.15 V	Ni-S	4.9 ± 0.5	2.30 ± 0.01	8.7 ± 1.7	-3.7 ± 1.9	0.013

[a]CN: coordination number; [b]R: bond distance; [c]σ^2: Debye-Waller factors; [d]ΔE_0: the inner potential correction. R factor: goodness of fit. * The experimental EXAFS fit of metal foil by fixing CN as the known crystallographic value.

1 **Supplementary Table 4**. Raman spectra of different nickel sulfides.

	Raman Peaks (cm^{-1})								
NiS_2	274.4	284.8	479.3						
Ni_3S_2	187.6	202.1	223.6	303.6	324.6	350.3			
Ni_3S_4	223.3	286.6	337.6	380.3					
α-NiS	147.4	165.6	174.7	222.3	285.1	333.4	374.9		
β-NiS	143.1	178.9	206.1	221.9	244.6	283.7	297.8	349.2	370.6

2

3

4

5

6

7

8

9

10

11

12

13

14

15

16

17

18

19

20

21

22

23

24

25

26

27

28

Supplementary Table 5. In-situ Raman spectra of $Ni_{1-x}Fe_xS_2$.

	Raman Peaks (cm^{-1})						
$x = 0$, 0.4 V	272.9	284.1	478.4				
$x = 0$, 0.3 V	271.5	281.2	478.4				
$x = 0$, 0.2 V	269.3	279.7	474.2				
$x = 0$, 0.1 V	268.6	277.0	473.5				
$x = 0$, 0.05 V	185.5	197.6	220.1	302.2	322.1	348.3	473.2
$x = 0$, -0.15 V	184.8	194.0	219.0	302.1	321.1	347.2	
$x = 0$, -0.25V	182.8	194.4	215.3	299.2	320.7	346.6	
$x = 0.1$, 0.4 V	273.5	283.2	478.9				
$x = 0.1$, 0.3 V	271.3	282.1	476.6				
$x = 0.1$, 0.2 V	270.1	280.2	474.5				
$x = 0.1$, 0.15 V	185.1	198.5	219.2	302.1	321.9	349.2	474.4
$x = 0.1$, 0.1 V	186.9	197.8	219.6	302.7	321.7	348.7	474.1
$x = 0.1$, -0.15 V	187.4	197.8	218.9	302.6	321.3	347.8	
$x = 0.1$, -0.25V	186.5	196.7	217.6	301.4	320.4	346.8	
$x = 0.2$, 0.4 V	274.2	285.0	479.8				
$x = 0.2$, 0.3 V	274.3	283.8	478.8				
$x = 0.2$, 0.25 V	271.3	282.5	476.5				
$x = 0.2$, 0.2 V	181.8	195.5	216.2	297.7	320.9	345.3	476.3
$x = 0.2$, 0.0 V	182.4	195.5	218.7	297.7	320.3	345.3	476.1
$x = 0.2$, -0.15 V	184.4	198.1	218.1	299.7	320.3	347.9	
$x = 0.2$, -0.25V	182.3	195.6	217.9	300.4	320.5	347.1	
$x = 0.25$, 0.4 V	276.2	285.9	480.8				
$x = 0.25$, 0.3 V	272.9	282.6	478.3				
$x = 0.25$, 0.25 V	271.6	281.9	476.9				
$x = 0.25$, 0.2 V	181.1	194.7	216.7	298.4	319.8	345.3	476.5
$x = 0.25$, 0.0 V	182.9	195.3	217.3	298.4	318.6	345.3	476.3
$x = 0.25$, -0.15 V	183.9	195.1	218.9	299.9	322.4	347.6	
$x = 0.25$, -0.25V	182.1	197.4	219.7	301.1	320.5	346.8	
$x = 0.33$, 0.4 V	273.5	283.8	478.4				
$x = 0.33$, 0.3 V	272.9	283.2	478.3				
$x = 0.33$, 0.25 V	270.6	282.1	476.0				
$x = 0.33$, 0.2 V	182.6	197.6	218.7	301.1	321.0	346.1	475.4
$x = 0.33$, 0.0 V	187.2	200.1	220.2	301.9	322.1	347.1	
$x = 0.33$, -0.15 V	185.1	198.2	219.7	300.5	320.5	347.1	
$x = 0.33$, -0.25V	181.1	197.2	220.2	301.1	321.4	347.4	

2

3

1 **Supplementary Table 6**. The DFT calculated energy of Ni $3d$ band center and S $3p$ band center of $Ni_{1-x}Fe_xS_2$
2 (x = 0.0, 0.1, 0.2 and 0.33) relative to Fermi level.

	Ni $3d$ (eV)	S $3p$ (eV)	Ni $3d$ - S $3p$ (eV)
x = 0.0	-2.204	-5.232	3.028
x = 0.1	-2.245	-4.888	2.643
x = 0.2	-2.318	-4.856	2.538
x = 0.33	-2.384	-4.788	2.404

3
4
5
6 **Supplementary Table 7**. The sulphur vacancy formation enthalpy ΔHf, Vs of $Ni_{1-x}Fe_xS_2$ (x = 0.0, 0.1, 0.2
7 and 0.33).

	Energy (eV)	μ_i (eV)	ΔHf, Vs (eV)
NiS_2	-289.10		
NiS_2 - V_S	-284.12	-4.12	0.86
$Ni_{0.9}Fe_{0.1}S_2$	-295.69		
$Ni_{0.8}Fe_{0.2}S_2$ - V_S	-290.74	-4.12	0.83
$Ni_{0.8}Fe_{0.2}S_2$	-302.33		
$Ni_{0.8}Fe_{0.2}S_2$ - V_S	-297.46	-4.12	0.75
$Ni_{0.67}Fe_{0.33}S_2$	-309.07		
$Ni_{0.67}Fe_{0.33}S_2$ - V_S	-303.76	-4.12	1.19

8
9
10
11
12
13

Supplementary Table 8. The formation energy of $Ni_{1-x}Fe_xS_2$ ($x = 0.0$ and 0.2) for reconstruction

Structure	NiS_2	Ni_3S_2	20%Fe@NiS_2	4%Fe@Ni_3S_2	FeS_2	S
Formula	Ni_4S_8	Ni_9S_6	$Fe_4Ni_{16}S_{40}$	$FeNi_{23}S_{16}$	Fe_2S_4	S_{32}
Energy (eV)	-58.207	-80.422	-304.213	-216.76	-36.139	-131.949
Normalization (eV)	-14.552	-26.807	-15.217	-27.095	-18.070	-4.123
Formation Energy (eV)		0.059 eV (E_{f1}) 0.025 eV (E_{f3})		0.036 eV (E_{f2})		

$$NiS_2 = 1/3\ Ni_3S_2 + 4/3\ S \tag{1}$$

$$E_{f1}' = 1/3\ E(Ni_3S_2) + 4/3\ E(S) - E(NiS_2) = 0.118\ eV$$

$$E_{f1} = 0.059\ eV$$

$$Fe_{0.2}Ni_{0.8}S_2 = Fe_{0.035}Ni_{0.8}S_{0.56} + 0.165\ FeS_2 + 1.11\ S \tag{2}$$

$$E_{f2}' = E(4\%Fe@Ni_3S_2) + 0.165\ E(FeS_2) + 1.11\ E(S) - E(20\%Fe@NiS_2) = 0.072\ eV$$

$$E_{f2} = 0.036\ eV$$

$$Fe_{0.2}Ni_{0.8}S_2 = 4/15\ Ni_3S_2 + 1/5\ FeS_2 + 16/15\ S \tag{3}$$

$$E_{f3}' = 4/15\ E(Ni_3S_2) + 1/5\ E(FeS_2) + 16/15\ E(S) - E(20\%Fe@NiS_2) = 0.050\ eV$$

$$E_{f3} = 0.025\ eV$$

This result is a value normalized to NiS_2 or $Fe_{0.2}Ni_{0.8}S_2$. For convenience of expression, the result normalized to a single sulphur atom as $E_{fn} = E_{fn}'/2$.

The reconstruction process is discussed in three cases. The first case is the NiS_2 phase transition to generate Ni_3S_2 with the sulphur leaching, as shown in Equation 1. For $Fe_{0.2}Ni_{0.8}S_2$, the segregation process (D. J. Vaughan and J. R C. *Mineral chemistry of metal sulfides*. Cambridge University Press, 1978, 62-66) exists in the phase transition process. Therefore, it is difficult to accurately

measure the Fe content in the final products with suitable characterization methods. We assume that there are two cases in which all Fe is segregated into FeS_2 (as shown in equation 3), and eventually retain some Fe, so proceed according to equation 2.

According to the test results of the EDS element ratio and XPS results, it can be known that with the extension of the test time, the Fe element will correspondingly leach with the phase transition process, and it will eventually stabilize at about 4% in the new reconstructed structure in 100 h long-term operation. Because the loss of sulphur is large, we assume that during the Fe loss process, it is extracted from the phase of $Ni_{0.8}Fe_{0.2}S_2$ is in the form of FeS_2 to forming new reconstructed structure, and the phase transition reaction are shown in equation (2) and (3). As E_{f3} (0.025 eV) or E_{f2} (0.036 eV) < E_{f1} (0.059 eV), so we have the result that Fe substitution can facilitate the phase transition to form the finalized structure.

Supplementary Table 9. In-situ Raman spectra of α-NiS, β-NiS and Ni_3S_4.

|	Raman Peaks (cm^{-1})						
β - NiS, 0.4 V	181.1	198.5	222.2	242.8	297.8	348.2	368.5
β - NiS, 0.2 V	176.4	193.4	222.7	242.8	296.4	346.8	368.1
β - NiS, 0.15 V	173.3	192.5	221.9	242.8	296.5	346.8	368.1
β - NiS, 0.1 V	178.8	193.0	215.0	237.3	296.7	319.1	343.8
β - NiS, -0.15 V	178.1	194.6	215.3	299.7	319.4	343.8	
β - NiS, -0.25 V	180.7	195.7	216.1	297.5	320.4	344.6	
α - NiS, 0.4 V	164.9	175.7	221.9	285.4	347.8		
α - NiS, 0.2 V	175.2	220.9	284.4	346.9			
α - NiS, 0.1 V	170.8	220.4	284.2	345.6			
α - NiS, 0.05 V	182.2	195.2	217.1	299.1	319.2	346.1	
α - NiS, -0.15 V	179.8	194.5	216.0	298.4	320.4	346.8	
α - NiS, -0.25 V	181.5	195.8	217.1	297.9	321.0	346.9	
Ni_3S_4, 0.4 V	223.1	286.3	338.5	381.5	480.9		
Ni_3S_4, 0.2 V	222.1	285.3	337.1	380.8	478.2		
Ni_3S_4, 0.1 V	220.1	284.2	335.6	379.1	477.6		
Ni_3S_4, 0.05 V	183.5	196.2	217.9	301.6	318.7	346.2	
Ni_3S_4, -0.15 V	184.1	196.5	219.4	300.2	320.3	346.5	
Ni_3S_4, -0.25 V	185.1	197.9	219.9	302.0	322.4	348.4	
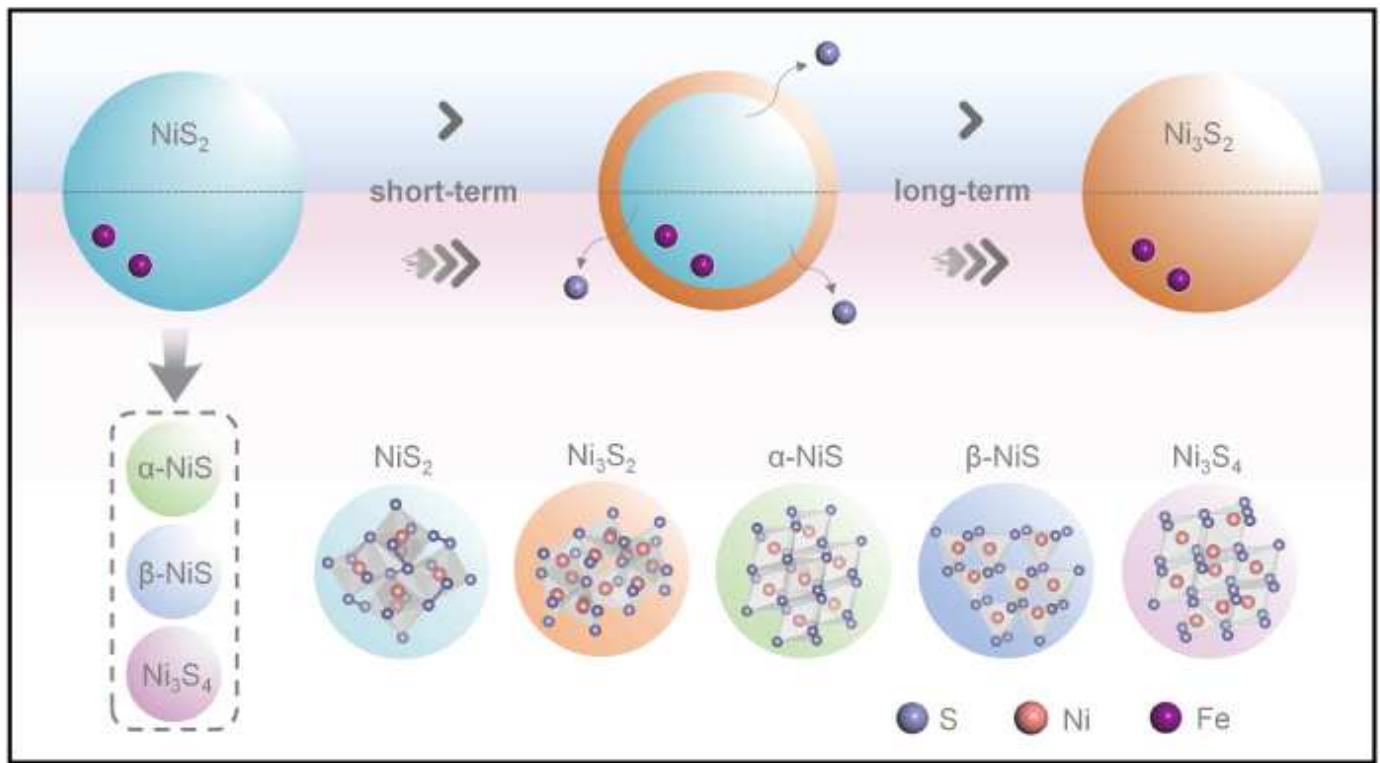
Figures

Figure 1

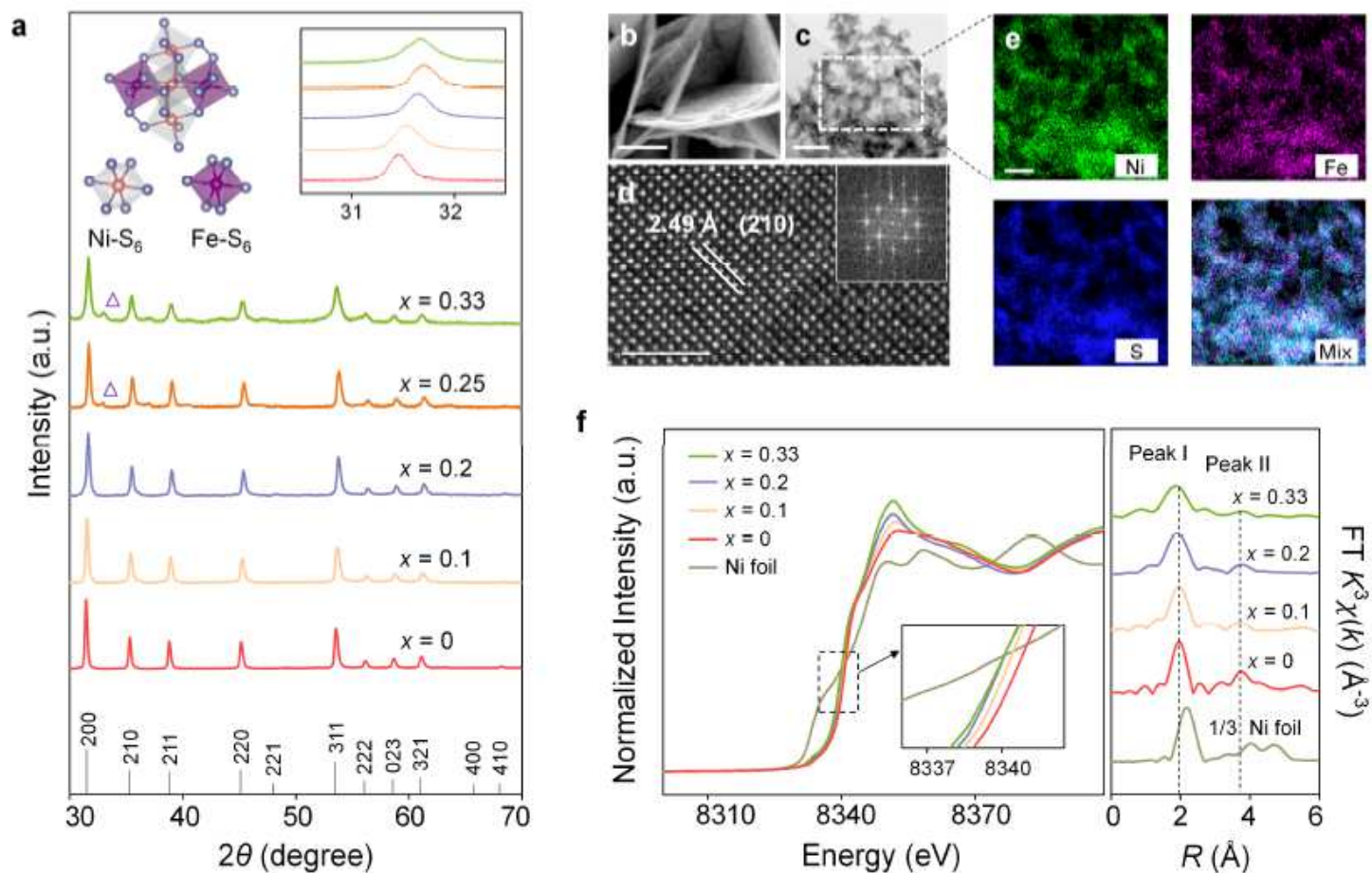Schematic illustration of dynamic reconstruction of multivalent nickel sulfide HER catalysts.

Figure 2

Structural characterizations of as-prepared Ni1-xFexS2 catalysts. a, Powder XRD patterns of synthesized Ni1-xFexS2 (x ≈ 0~0.33) samples. Inset, schematics of the composition of Fe substituted nickel disulfides and the magnified XRD patterns in the range between 30 and 33. The triangle symbols represent diffraction peak of FeS2 structure. b, Top-view SEM image of the Ni0.8Fe0.2S2. Scale bar, 1 μm. c, TEM image of Ni0.8Fe0.2S2. Scale bar, 100 nm. d, High-resolution TEM image of Ni0.8Fe0.2S2. Scale bar, 2 nm. The fast Fourier transform is shown in the inset of (d) confirms the crystalline nature of the bulk material. e, The corresponding EDS elemental mappings of Ni, Fe, S and the mixed elemental mapping. Scale bar, 50 nm. f, Normalized Ni K-edge XANES analysis (left axis) of Ni1-xFexS2 samples with Ni foil as reference, as well as the corresponding k3-weighted Fourier transform (FT) Ni K-edge EXAFS spectra (right axis). Inset, Magnified pre-edge XANES region. Peaks I and II in the FT-EXAFS plots are assigned to Ni-S and Ni-Ni radial distances, respectively.
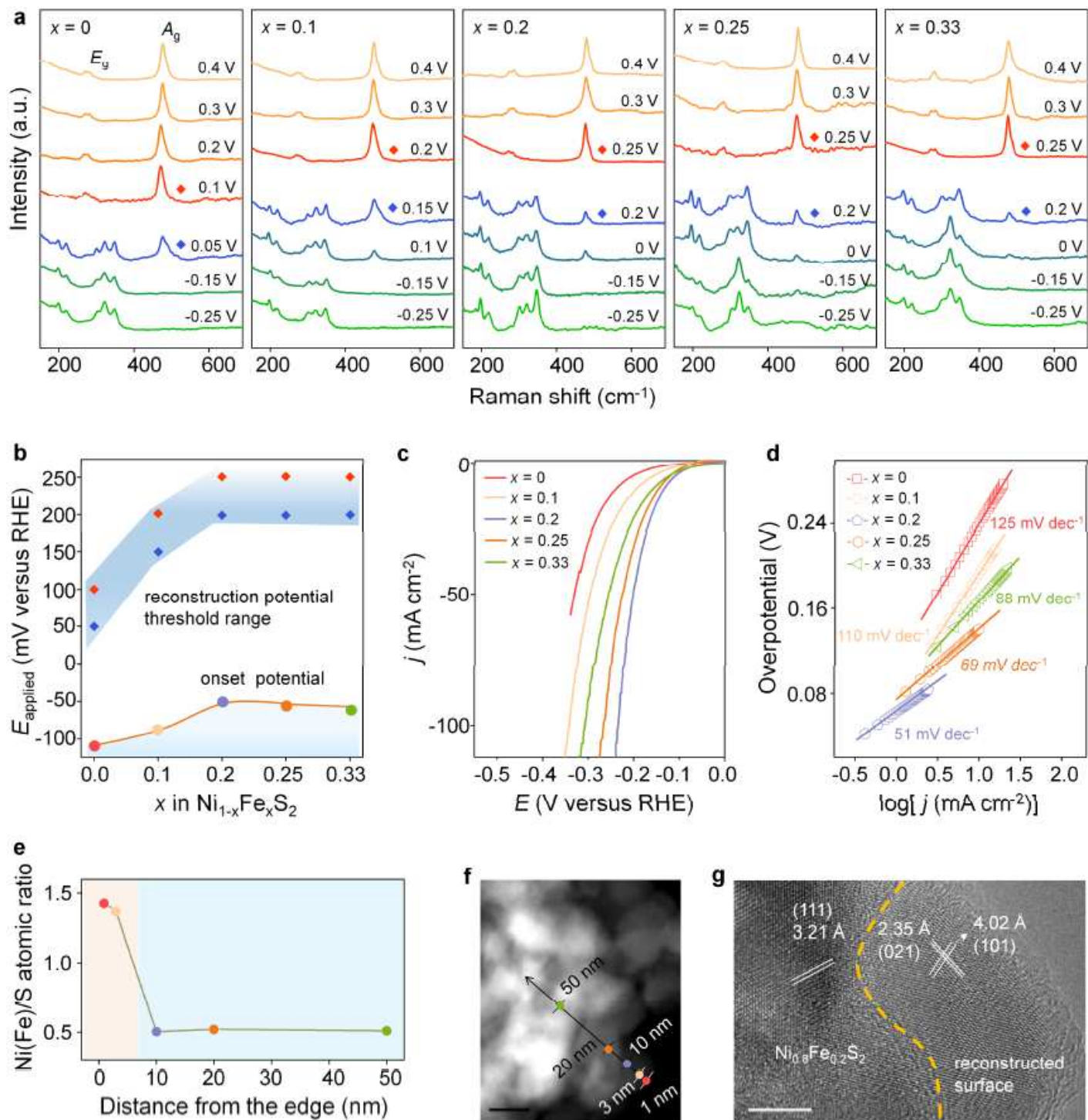
Figure 3

In-situ investigation of dynamic surface reconstruction process and HER performances of catalysts. a, In-situ Raman spectra of Ni1-xFexS2 (x ≈ 0~0.33) samples at the potentials of 0.4~-0.25 V versus reversible hydrogen electrode (vs. RHE) in 1M KOH. b, The surface reconstruction potential threshold range for Ni1-xFexS2 (x ≈ 0~0.33) samples, and the corresponding onset potentials of hydrogen evolution are plotted to show the dynamic correlation of structure-activity. The red diamond dots represent the final potential of existence for Raman peaks of Ni1-xFexS2 structures, and the blue diamond dots stand for the

potential of emerging of Ni3S2 Raman peaks. c, HER polarization curves of Ni1-xFexS2 catalysts on carbon fiber paper in N2-saturated 1M KOH at a scan rate of 5 mV s-1, d, Corresponding HER Tafel plots derived from the polarization curves. e, f, Elemental composition of post-electrolysis Ni0.8Fe0.2S2 determined from EDS at a series of spots along a line from the crystallite edge to the bulk reveals the variation in Ni(Fe):S composition across the crystallite, the marked points in (f) denote the scanning distance along the pathway in nm. g, HRTEM image of post-electrolysis Ni0.8Fe0.2S2. The scale bars are 20 nm in (f), 5 nm in (g).
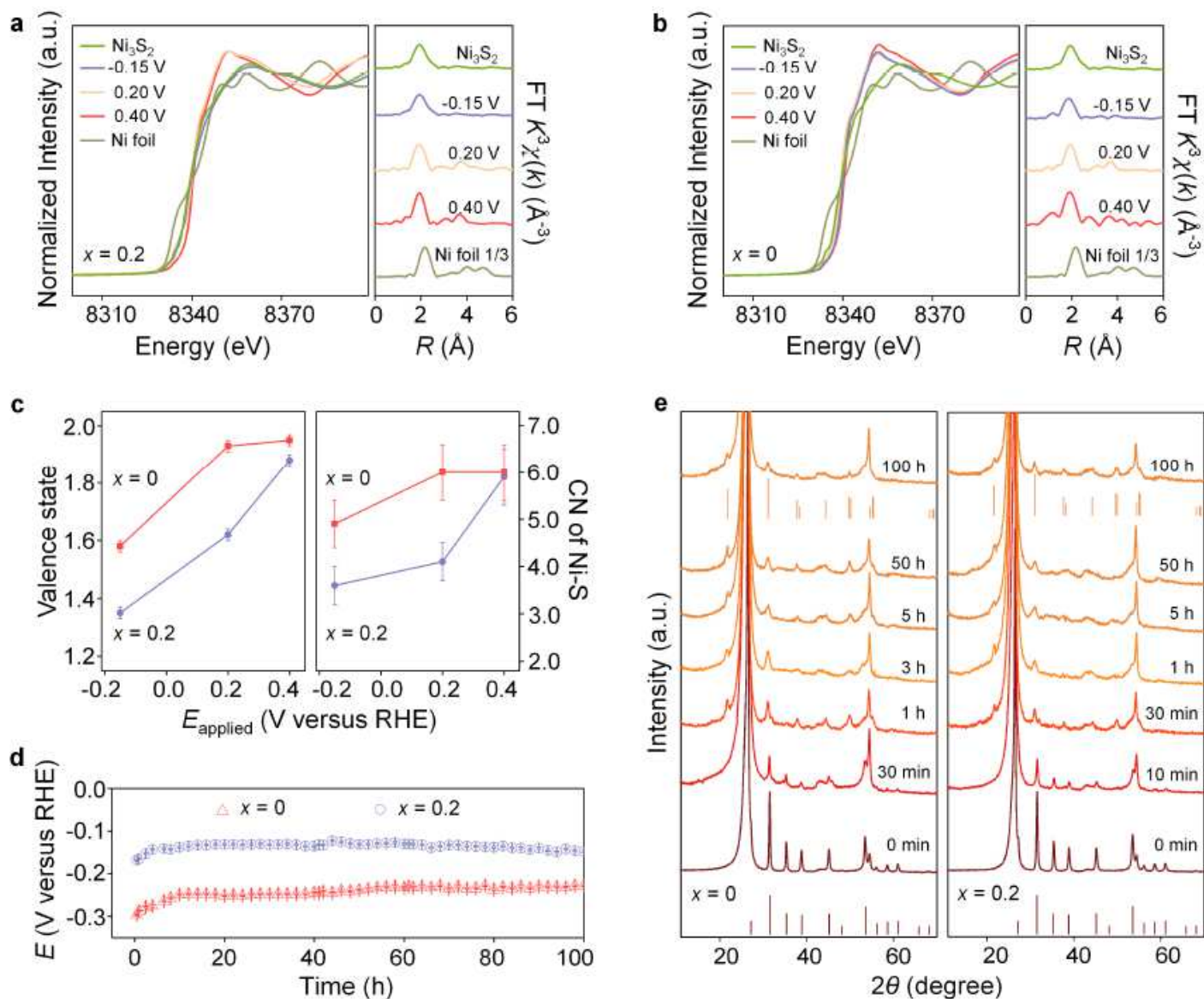

Figure 4

Operando XAFS spectra and long-term operation characterization of catalysts. a, b, Normalized operando Ni K-edge XANES analysis (left axis) at 0.40, 0.20, and -0.15 V (vs. RHE) with Ni Foil and standard Ni3S2 powder (Alfa Aesar) as reference, as well as the corresponding operando FT k3-weighted Ni K-edge EXAFS (right axis): Ni0.8Fe0.2S2 (a) and NiS2 (b). c, Left axis, the fitted average valence states of nickel element from XANES spectra for NiS2 and Ni0.8Fe0.2S2. Error bars represent the standard deviation from

at least three independent measurements. The right axis show the changes of coordination number (CN) for Ni-S corresponding to the applied potentials. d, Chronopotentiometric curves obtained with Ni0.8Fe0.2S2 and NiS2 at constant current density of 10 mA cm-2. e, XRD patterns of catalysts after the operation of HER instantly at 10 mA cm-2 during 100 h. The 2θ peaks of ~26.5° and 54.5° stand for the carbon fiber paper substrates.
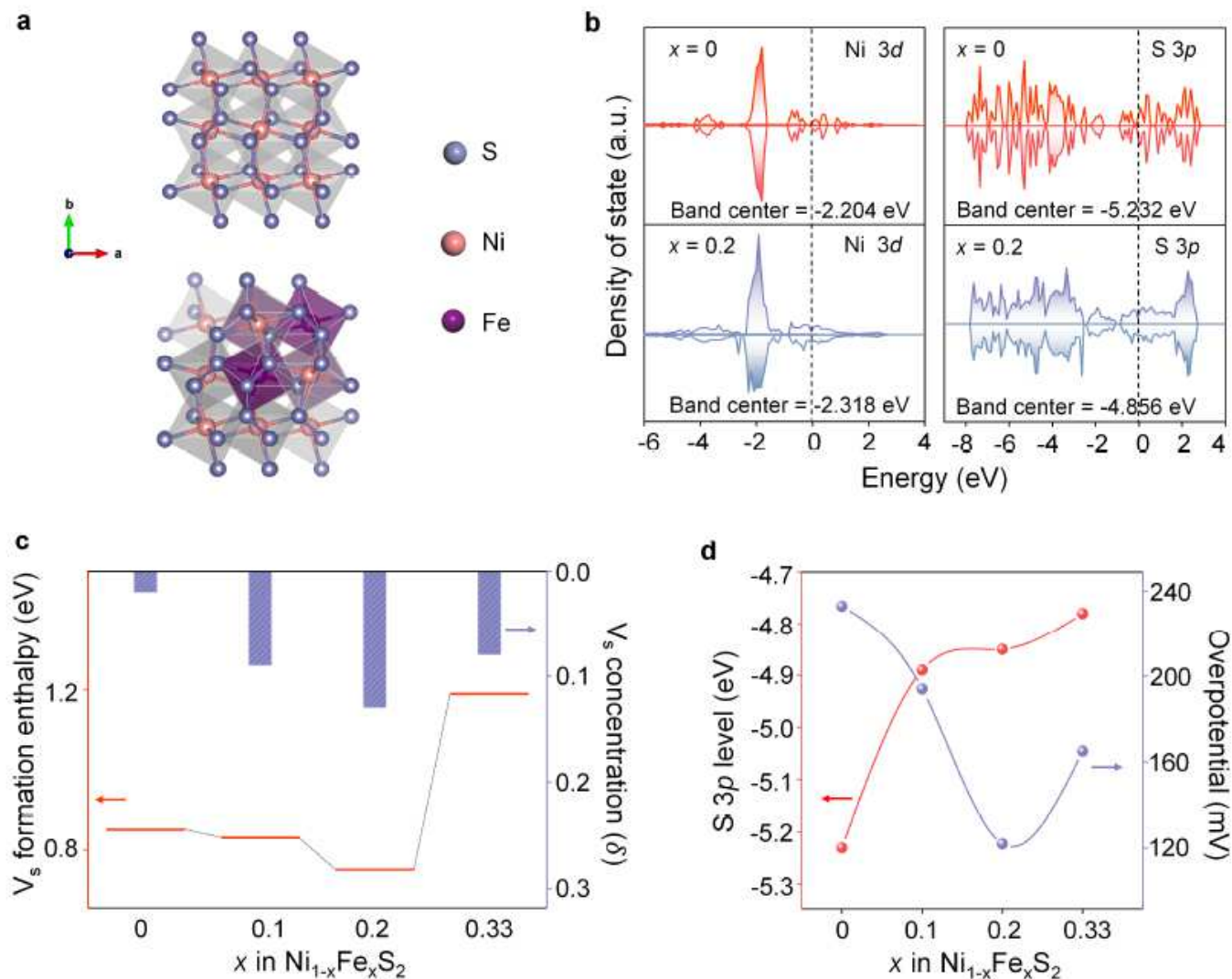

Figure 5

Electronic interpretation of the effect of Fe substitution on catalyst evolution. a, Computational models of Ni1-xFexS2: top, x = 0; bottom, x = 0.2. b, Computed Ni 3d, S 3p PDOS of Ni1-xFexS2 (x = 0.0, 0.2). c, Calculated sulphur vacancy (VS) formation enthalpy and sulphur vacancy concentration (δ) of the samples for Ni1-xFexS2 (x = 0.0, 0.1, 0.2, 0.33). d, Computed S 3p PDOS related to the overpotential of Ni1-xFexS2 (x = 0.0, 0.1, 0.2, 0.33) @ 10 mA cm-2.
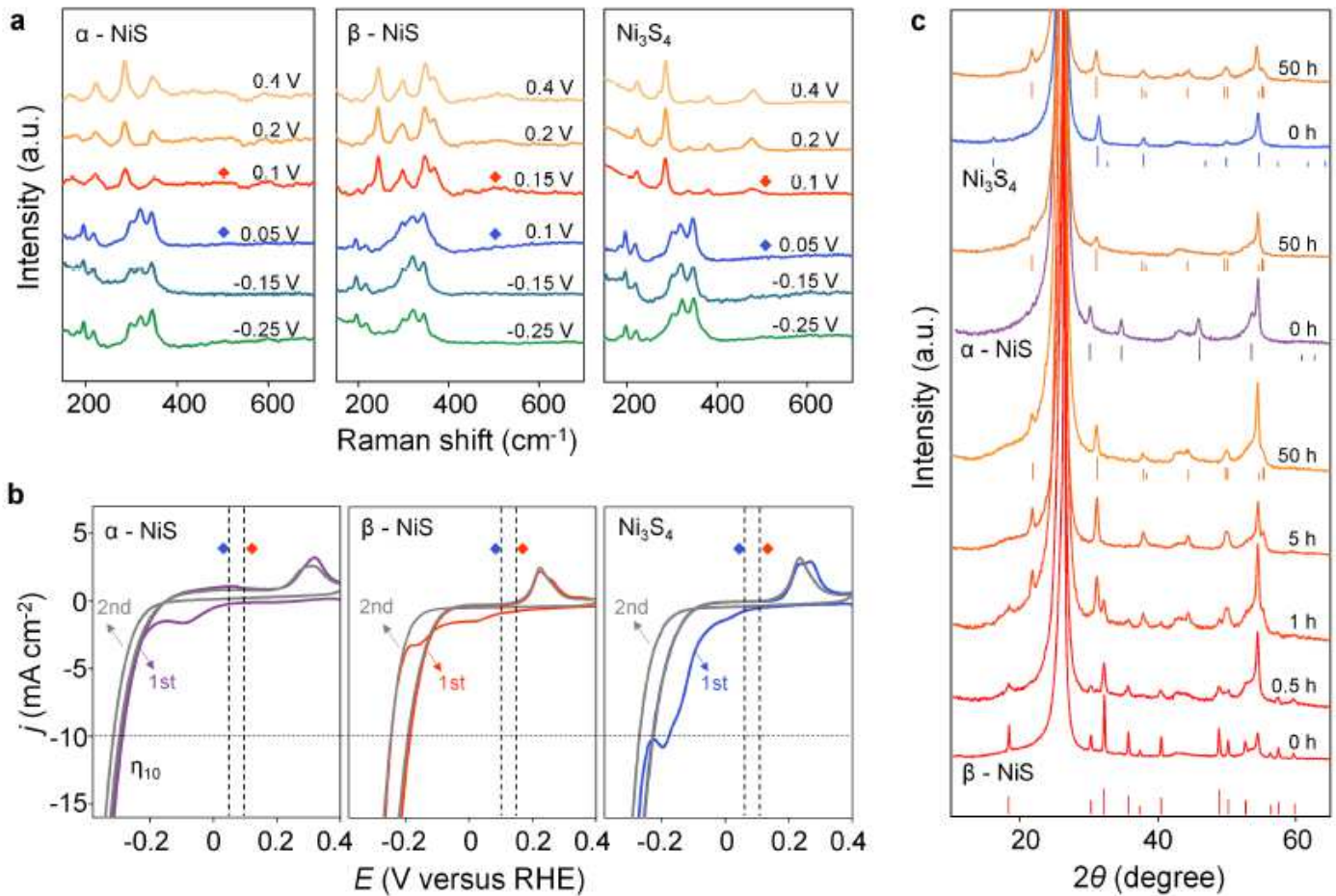
Figure 6

Dynamic structural evolution characterization of α-NiS, β-NiS and Ni3S4 catalysts. a, In-situ Raman spectra of nickel sulfides at the potentials of 0.4~-0.25 V (vs. RHE) in 1M KOH for α-NiS, β-NiS and Ni3S4. b, Cyclic voltammetry curves of α-NiS, β-NiS and Ni3S4 in N2-saturated 1 M KOH with a scan rate of 2 mV s-1 between 0.4 and -0.4 V (vs. RHE). The red diamond dots represent the final potential of existence for α-NiS, β-NiS and Ni3S4 Raman peaks, and the blue diamond dots stand for the potential of emerging of Ni3S2 Raman peaks. c, XRD patterns of catalysts after the operation of HER instantly at constant current density of 10 mA cm-2.